F. Vignati, A. Guardone
Dynamics of Cylindrical Converging Shock Waves Interacting with Aerodynamic Obstacle Arrays
Physics of Fluids, Vol. 27, N. 6, 2015, 066101 (27 pages)
doi:10.1063/1.4921680

Dynamics of cylindrical converging shock waves interacting with aerodynamic obstacle arrays

F. Vignati[1] and A. Guardone[1, a)]
Department of Aerospace Science and Technology, Politecnico di Milano
via La Masa, 34 - 20156 Milano, Italy

(Dated: 12 May 2015)

Cylindrical converging shock waves interacting with an array of aerodynamic obstacles are investigated numerically for diverse shock strengths and for different obstacle configurations in air in standard conditions. The considered number of obstacles N is 4, 6, 8, 16 and 24. Obstacles are lenticular airfoils with a thickness-to-chord ratio t/c of 0.07, 0.14 and 0.21. The distance of the airfoil leading edge from the shock focus point r_{LE}/r_{LE}^{ref} is 1, 2, 2.5, where $r_{LE}^{ref} = 7$ is the dimensionless reference distance from the origin. Considered impinging shock Mach number M_s are 2.2, 2.7 and 3.2 at the reference distance from the origin. The reference experimental configuration ($N = 8, t/c = 0.14, r_{LE} = 7, M_s = 2.7$) was proposed by M. Kjellander, N. Tillmark, N. Apazidis, Phys. of Fluids **22**, 046102 (2010). Numerical results compare fairly well to available one-dimensional models for shock propagation and to available experimental results in the reference configuration. Local reflection types are in good agreement with the classical criteria for planar shock waves. The main shock reshaping patterns are identified and their dependence on the shock strength and obstacle configuration is exposed. In particular, different shock patterns are observed after the leading edge reflection, which results in polygonal shock wave with N, $2N$, $3N$ and $4N$ sides. The largest temperature peak at the origin is obtained for the 8- and the 16-obstacle configurations and for the smallest thickness to length ratio, 0.07, located at distance from the origin of $2r_{LE}^{ref}$. In terms of compression efficiency at the origin, the 16-obstacle configuration is found to perform slightly better than the reference 8-obstacle configuration—with an efficiency increase of about 2-3%, which is well within the model accuracy—thus confirming the goodness of the obstacle arrangement proposed by Kjellander and collaborators.

PACS numbers: 47.40.Nm, 47.40.Ki
Keywords: Converging shock waves; Aerodynamic obstacles; Shock reshaping; Ideal gas; Inviscid compressible flows

I. INTRODUCTION

Imploding shock waves of either cylindrical and spherical shape are currently being investigated in connection with fundamental studies of shock front instabilities[1] as well as effective means to produce high pressure and temperature conditions at the focus point, where peculiar physical phenomena can be observed, including sonoluminescence.[2] Moreover, in Inertial Confinement Fusion (ICF), high energy concentration are required to ignite the fuel pallet and start the fusion reaction.[3] Unfortunately, surface corrugation instabilities may occur and reduce the effectiveness of converging cylindrical and spherical shocks, causing a mayor reduction of the temperature and pressure values observed at the focus point.[1,4–7] The onset of instabilities in curved converging shocks eventually prevent their applications to ICF problems.

Diverse theoretical, numerical and experimental investigations[8–13] demonstrate that if an array of obstacles is located along the shock path, the interaction between the shock wave and the obstacles can possibly result in the reshaping of the shock geometry into a more stable configuration. Nevertheless, during the reshaping process, non negligible losses occur that reduce the shock strength and therefore care must be taken in identifying the suitable compromise between front stability and shock effectiveness.[12]

The present work moves from the experimental study by Kjellander, Tillmark and Apazidis,[13] who explored the interaction between cylindrical shocks and an array of eight aerodynamic obstacles in dilute air. Numerical simulations are performed here to explore a wider range of geometrical configurations and operational parameters, with the purpose of finding alternative, more efficient, solutions. Parametric studies on the reshaping of shock waves were performed in a shock tube in Ref. 14. The purpose of the present study is the numerical investigation of the dynamics of converging cylindrical shock waves as they interact with arrays of aerodynamic obstacles. Details on the numerical scheme and a short assessment of the space and time integration parameters are given in section III B 1 and the method for determining the shock position at each time step is also described (sec. III B 4).

The present study aims at providing a preliminary assessment of the diverse gas-dynamics phenomena and at identifying the relevant parameters. In particular, the study focuses on the evaluation of the pressure and temperature peaks at the focus point (sec. IV A) and the assessment of the diverse shock reflection patterns (sec. IV B). In detail, the type of leading edge reflection is assessed first (sec. IV B 1), including the leading edge triple point trajectories (sec. IV B 2). Note that, differently from planar shock theory,[15] the study of the reshaping of converging shock waves must cope with the shock unsteadiness, the occurrence of non-homogeneous shock-induced flows, the front curvature and other complex conditions which cause classical two-shock and three-shock theories to be inapplicable. The shock reshaping process fol-

a)Electronic mail: alberto.guardone@polimi.it

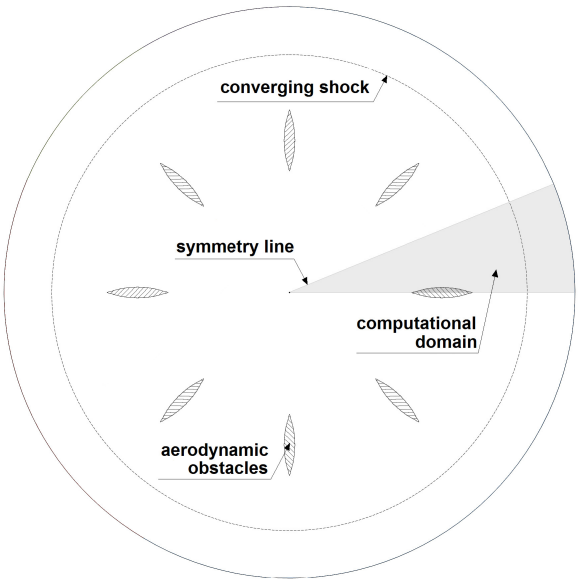

FIG. 1. Physical domain of propagation and reshaping of the converging shock wave for the reference configuration. The gray region is the computational domain.

lowing the leading edge reflection is studied (sec. IV B 3) and secondary reflections caused by the interaction of shock wave originating from different obstacles are investigated (sec. IV B 4). Past the obstacles, trailing-edge reflections and shock patterns are studied (sec. IV B 5), which result in a number of additional shock reflection prior to the focusing point (sec. IV B 6).

II. SHOCK RESHAPING PROCESS IN THE REFERENCE CONFIGURATION

The main features of the shock-obstacle interaction are presented in this section for the reference configuration described in Ref. 13. The geometry is depicted in figure 1, where a cylindrical shock wave converges towards the origin and it interacts with a symmetrical array of 8 aerodynamic obstacles with lenticular shape. A planar, two-dimensional section of the cylindrical shock is modeled. A further reduction of the computational domain is made possible thanks to the problem symmetry: simulations are performed in a sub-domain, delimited by two adjacent symmetry lines, spanning an angle of π/N, where N is the number of obstacles (the gray area in figure 1).

In accordance with Ref. 13, an inviscid representation of the flow field is chosen in the simulation. Therefore, viscous and thermal conductivity effects are not included in the simulations since they are assumed to be relevant only in the viscous and thermal bounday layers, whose thickness is assumed to be negligible with respect to the obstacle scale. Geometrical variables are made non dimensional with respect to the quantity $L = 0.01$m, in accordance with Ref. 13. Unless differently specified, all quantities (both geometrical and fluid-dynamical) are to be hereafter intended as non-dimensional. The distance of the leading edge from the focus point is $r_{LE}^{ref} = 7$. The dimensionless obstacle maximum thickness-to-chord ratio is $t/c = 0.14$, where the non-dimensional chord length is 5. The Mach number M_s of the impinging shock is equal to 2.7 slightly before the first shock-obstacle interaction, namely, at $r = r_{LE}^{ref}$. Note that the shock Mach number M_s and hence the shock strength increase as the shock front converges towards the origin.

According to Ref. 13, in the reference configuration the reshaping process is characterized by two main interactions with the obstacle, which are illustrated in figure 2. The first reflection takes place at the obstacle leading edge (termed first step, figure 2(a)). The shock undergoes a single Mach reflection, generating a triple point where the unperturbed portion of the incident shock, a reflected wave (termed *wave A*) and a Mach stem merge. From the three-shock theory, the three-wave system geometry varies with time: while the incident shock continues propagating inwards, the triple point moves away from the obstacle, and eventually approaches the symmetry line between two obstacles (second step, figure 2(b)).[15] Note that the three-shock theory strictly applies to straight shocks, but it is locally in good agreement with the present results concerning curved shock fronts.

Afterwards, the Mach stem generated by the leading edge reflection impinges against the symmetry line and undergoes a *secondary reflection* of Mach type, which generates an additional three-shock structure including a new Mach stem and a reflected wave (*wave B*, third step, figure 2(c)). After the secondary triple point reached either the obstacle or the bottom symmetry line (figure 2(d)), the converging shock consists of a N-edges polygonal wave. Each side of the wave originates from the secondary Mach stem. The reshaping process may now be considered concluded. Both Mach stems exhibit a small outward curvature, similarly to what observed in Direct Mach Reflections (DiMR), but the concavity is negligible in the considered conditions and therefore the reshaped shock is said to be a polygonal one.

In the next section, alternative experimental configurations are devised from the reference one by varying both the obstacle layout and the operating conditions.

III. METHODOLOGY

A. The tested configurations

Preliminary simulations performed in reference conditions show a high sensitivity of the reshaped shock pattern with respect to small changes in the obstacle geometry and arrangement and on the initial conditions.

Physical factors, i.e. fluid dynamic parameters, include the shock intensity (M_s) and the fluid properties, i.e., the specific-heat ratio γ. Geometrical factors include the number of obstacles N, the thickness-to-chord ratio t/c and the non-dimensional radial coordinate of the obstacle leading edge r_{LE}. In the present section, a test matrix is identified by varying these parameter with respect to their reference values.

Considered parameter ranges are listed in table I. Each

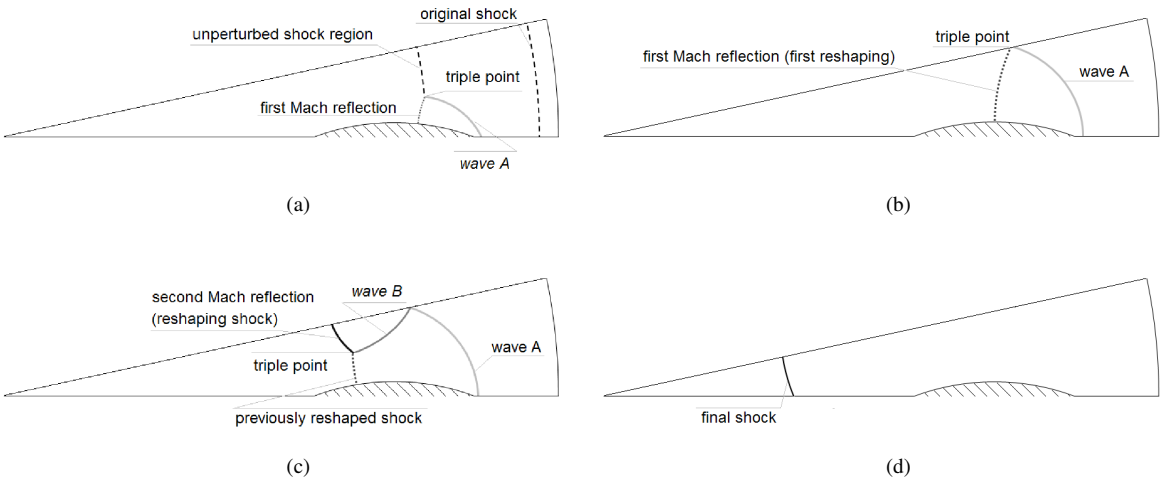

FIG. 2. Relevant features of the basic reflections causing the shock reshaping in the reference condition.

TABLE I. Test matrix for the numerical experiments. Considered parameters are the number of obstacles N, the thickness-to-chord ratio t/c, the radial coordinate of the obstacle leading edge r_{LE} and the shock Mach number M_s. In all tests, the operating fluid is air in standard conditions, with $\gamma = 1.4$. The value that the parameter assumes in the reference configuration in Ref. 13 is evidenced in bold style.

Number of obstacles	N	6	**8**	16
Thickness-to-chord ratio	t/c	0.07	**0.14**	0.21
Leading edge coordinate	r_{LE}	**7**	14	17.5
Shock Mach number at r_{LE}^{ref}	M_s	2.2	**2.7**	3.2

configuration is characterized by four parameters: the obstacle number, the obstacle thickness-to-chord ratio, the leading edge radius and the shock Mach number at the time the implosion starts interacting with the obstacle. Each parameter is influential on the reshaping process and introduces a trade-off in the research of the optimal configuration. For large obstacle numbers N, indeed, the resulting polygonal shock is more similar to a cylindrical wave, but the number of reflections, and therefore the losses, are higher. Obstacles with a low thickness-to-chord value introduce weaker perturbations in the flow field than thicker obstacles, resulting in lower losses, but also in the necessity of a larger number of obstacles in order to complete the reshaping before the shock wave reaches the focus point. The effect of the obstacle distance from the focus point is two-fold: on the one hand, the larger r_{LE} is, the larger is the expected number of reflections downstream the obstacle. On the other hand, the blockage effect on the inter-obstacle channel is lower. The pressure jump across the shock wave increases with M_s, and therefore the effectiveness of the shock wave is expected to be higher if the shock wave is more intense. Nevertheless, a preliminary analysis suggests that M_s grows less-than-linearly with β_P, and therefore the overall efficiency of the process decreases.

In the present work, obstacles are arranged in arrays of six, eight and sixteen obstacles, each placed at once, twice and 2.5 times the reference values of the non-dimensional radial coordinate of the leading edge, that is, 7. This range is established after a preliminary analysis, and is limited below by geometrical interference and above by a weak dependence of integral quantities on the obstacles position itself. Moreover, due to the heavy computational cost of the simulations, preliminary simulations are performed with different values of N in order to highlight the most convenient range (sec. IV A).

The shape of lenticular flow dividers is defined as a double circular arc with sharp leading and trailing edges. Thickness-to-chord ratios are equal to $t/c = 0.14$ (reference condition) ±50%. The reference Mach number of the shock M_s at the impingement on an obstacle at reference distance is 2.7. This value is varied on three levels (reference M_s, ±20%): 2.2, 2.7 and 3.2. As demonstrated by Guderley[16], the Mach number of a converging shock wave increases during the convergence, depending on time with a power law. Therefore, due to the acceleration, the shock cannot be characterized only by means of M_s, because the shock parameters change along time and therefore vary with the obstacle leading edge position during the propagation of the wave. In the following, therefore, shocks are identified by means of the parameter β_P, which is the pressure ratio across the initial discontinuity (see paragraph III B 1). The correspondence between the initial pressure ratio β_P and the shock Mach numbers at diverse r_{LE} is listed in table II. In addition, the case with no obstacles is also investigated for reference and the 24-obstacle case is partially explored (see sec. IV).

B. Computational Fluid Dynamics Model

Numerical simulations are carried out using a multi-domain approach that was devised by the authors[17] and it is briefly recalled here in section III B 1 for completeness. The dependence of the results on the grid spacing and on the time-step is assessed in III B 2. In section III B 3, the assumption of perfect thermal behavior is discussed for the considered cases.

TABLE II. Correspondence matrix between the initial pressure ratio β_P and the shock Mach number slightly before the obstacle leading edge for diverse r_{LE} values. The value that the parameter M_s assumes in the reference configuration in Ref. 13 is evidenced in bold style.

Initial pressure ratio β_P	11	16	27
Shock Mach number at $r_{LE} = 7$	2.2	**2.7**	3.2
Shock Mach number at $r_{LE} = 14$	2.0	2.5	3.0
Shock Mach number at $r_{LE} = 17.5$	1.9	2.4	2.9

Finally, in III B 4, numerical solutions are verified against analytic self-similar solutions and experimental data.

1. Multi-domain simulation approach

In the reference experimental configuration, the cylindrical shock wave in figure 1 results from the reshaping into a cylindrical shape of a planar shock wave, which is generated within a straight-axis shock tube. The reshaping occurs by forcing the shock through a duct at the closed end of the shock tube. Further details can be found in Ref. 13. The generation of cylindrical converging shock waves is discussed also in Refs. 18–21.

In the numerical experiments, the cylindrical converging shock is generated by the imposition of an axisymmetrical pressure step upstream the obstacle. The internal state (identified by still gas at pressure P_i and density ρ_i) is the same for all the simulations, while the initial external pressure P_e depends on the parameter $\beta_P = P_e/P_i$. The corresponding density is computed from the Hugoniot adiabate for a polytropic (constant specific heat) ideal gas as

$$\rho_e = \rho_i \cdot \frac{(\gamma+1/\gamma-1)\beta_P + 1}{(\gamma+1/\gamma-1) + \beta_P}.$$

Note that due to the curvature of the shock wave, the post-shock states changes in a continuous way as the shock moves towards the origin.

The above initial conditions result in the formation of a three-wave system including the converging shock wave, a converging contact discontinuity and a diverging rarefaction wave. The contact discontinuity is slower than the shock; therefore to obtain an isolated convergent shock wave the initial pressure step is located sufficiently far from the obstacles. It is observed that—for the explored Mach number range—the minimum distance between the pressure step and the center corresponds to at least five times the chord of the obstacles.

In order to reduce the computational time prior to the reshaping, simulations are divided into three separate parts according to the multi-domain approach described in Ref. 17. Prior to the impingement on the obstacles leading edges, the cylindrical shock wave is simulated by means of a dedicated solver for the Euler equations in a cylindrical coordinates system.[22]

The fully two-dimensional simulation of the shock reshaping and convergence process is performed on the slice of the domain illustrated in figure 1. The radius of the circular sector spans from zero up to the shock location. The shock tail is only partially included, which allows to reduce the number of nodes, and to neglect the contact discontinuity and rarefaction wave. The initial conditions for this second part are set by interpolating on the new grid the solution of the previous one-dimensional simulations.

A further interpolation step may be required if a large number of obstacles is used. In this case, a small area surrounding the focus point is removed from the two-dimensional computational domain, because elements with a vertex in the origin present an excessively large aspect ratio, which can jeopardize the accuracy of the calculation[17]. The simulation of the focusing is performed on a dedicated domain which includes the origin and a small circular region partially overlapping the previous computational domain. The angle in the origin is an integer multiple of π/N, usually $\pi/2$. The solution is linearly interpolated from the old mesh to the new one also in the non overlapping regions by exploiting the symmetry of the problem. Due to the reduced size of the domain, the additional time required by the interpolation and the simulation on a non-elementary slice is negligible. The detection of the shock position, that is necessary to trigger the domain interface, is achieved by applying the method described in section III B 4. For additional details on the simulation procedure, the reader is referred to Ref. 17.

2. Space and time integration of the flow model

Numerical simulations are carried out using the FlowMesh code, developed at the Department of Aerospace Science and Technology of Politecnico di Milano.[23,24] The solver is a standard finite-volume unstructured-grid solver; the unsteady Euler equations for compressible inviscid flows are solved by using a high-resolution flux (centered and Roe scheme, van Leer limiter, see Ref. 25) and by using the Backward Euler implicit time integration scheme. The latter is only first-order accurate and was preferred over the e.g. second- and third-order Backward Differentiation Formulæ for robustness.

The simulations are performed on a fixed grid with a number of grid nodes ranging from 50 000 to 400 000, depending on the computational domain size, with an a priori refinement in correspondence of the regions of interest, which include the obstacles leading and trailing edges, the shock reflection region and the focusing region.

The grid and time-step dependence is verified for a range of grid element sizes and time step levels, as reported in figures 3 and 4, respectively. The simulations were carried out considering $N = 16$, reference r_{LE} and t/c, and a higher shock Mach number $M_s = 4.7$, which is more demanding in terms of space and time resolution.

In figure 3, the non dimensional pressure profile over the bottom symmetry line and the obstacle surface is reported at four relevant time level, corresponding to the impinging shock being located at 25% (figure 3(a)), 50% (figure 3(b)), 75% (figure 3(c)) and 100% (figure 3(d)) of the obstacle chord. Five different grids are considered, with reference grid length

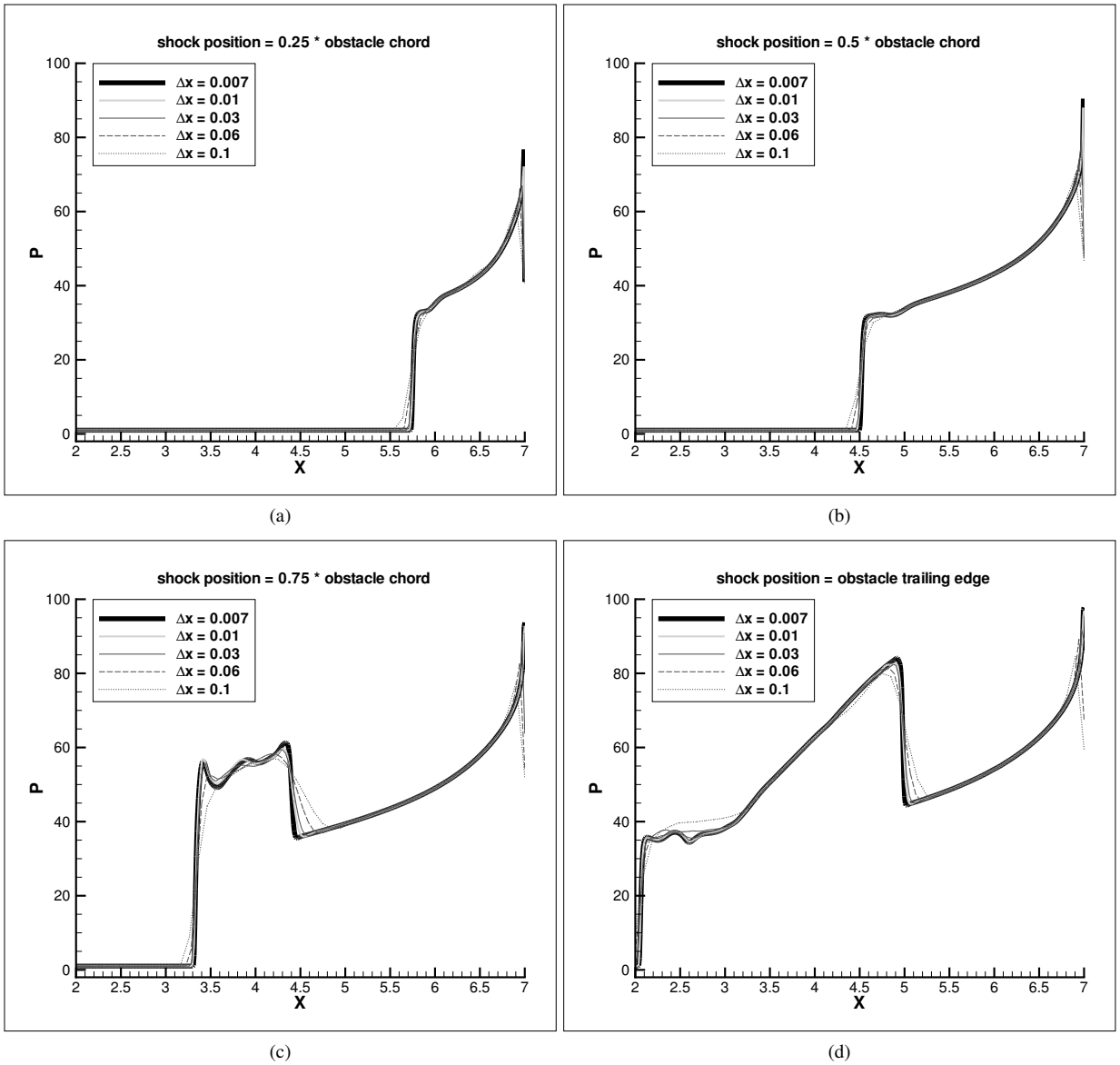

FIG. 3. Pressure—obtained with different meshes—on the obstacle during the propagation of a shock with Mach number of 4.7 at r_{LE}^{ref}. The time step is $\Delta\tau = 9 \times 10^{-4}$ in all simulations. The obstacle leading edge is at $r_{LE} = 7$. The shock displacement in each figure corresponds to 25% of the obstacle chord.

Δx ranging from 0.1 to 0.007, with Δx being the maximum element linear size. All simulations in figure 3 were carried out with a time step of 9×10^{-4}, that is the one adopted for all the simulations reported in section IV. The definition of non dimensional quantities P, T and τ is detailed in III B 3. The pressure profiles in figure 3 are found to be almost independent from the grid spacing for the three most refined grids, namely, $\Delta x = 0.03, 0.01, 0.007$.

In figure 4, the pressure profile over the bottom symmetry line and the obstacle surface is reported at the same four time levels as in figure 3 for six different values of the time-step $\Delta\tau$, ranging from 9×10^{-3} to 3×10^{-4}. All simulations in figure 4 were carried out over a grid made of 56 000 nodes ($\Delta x = 0.01$). The pressure profiles obtained with the three smallest time steps, $\Delta\tau = (3, 4.5, 9) \times 10^{-4}$, exhibit a satisfactory overlap.

Finally, figure 5 illustrates the dimensionless temperature profile over time at the focus point T_0 for different time and space discretizations. In particular, results in figure 5(a) are computed for different grids resolution using the same time step of $\Delta\tau = 9 \times 10^{-4}$; results in figure 5(b) are computed for different time steps over a grid with 56 000 nodes ($\Delta x = 0.01$). Not surprisingly, the accurate determination of the temperature profile at the focus point is the most demanding quantity in terms of grid and time-step resolution. Therefore, it is used here to select the grid and the time-step to be used in the following. The selected grid spacing and time step are $\Delta x = 0.01$ and $\Delta\tau = 9 \times 10^{-4}$ respectively.

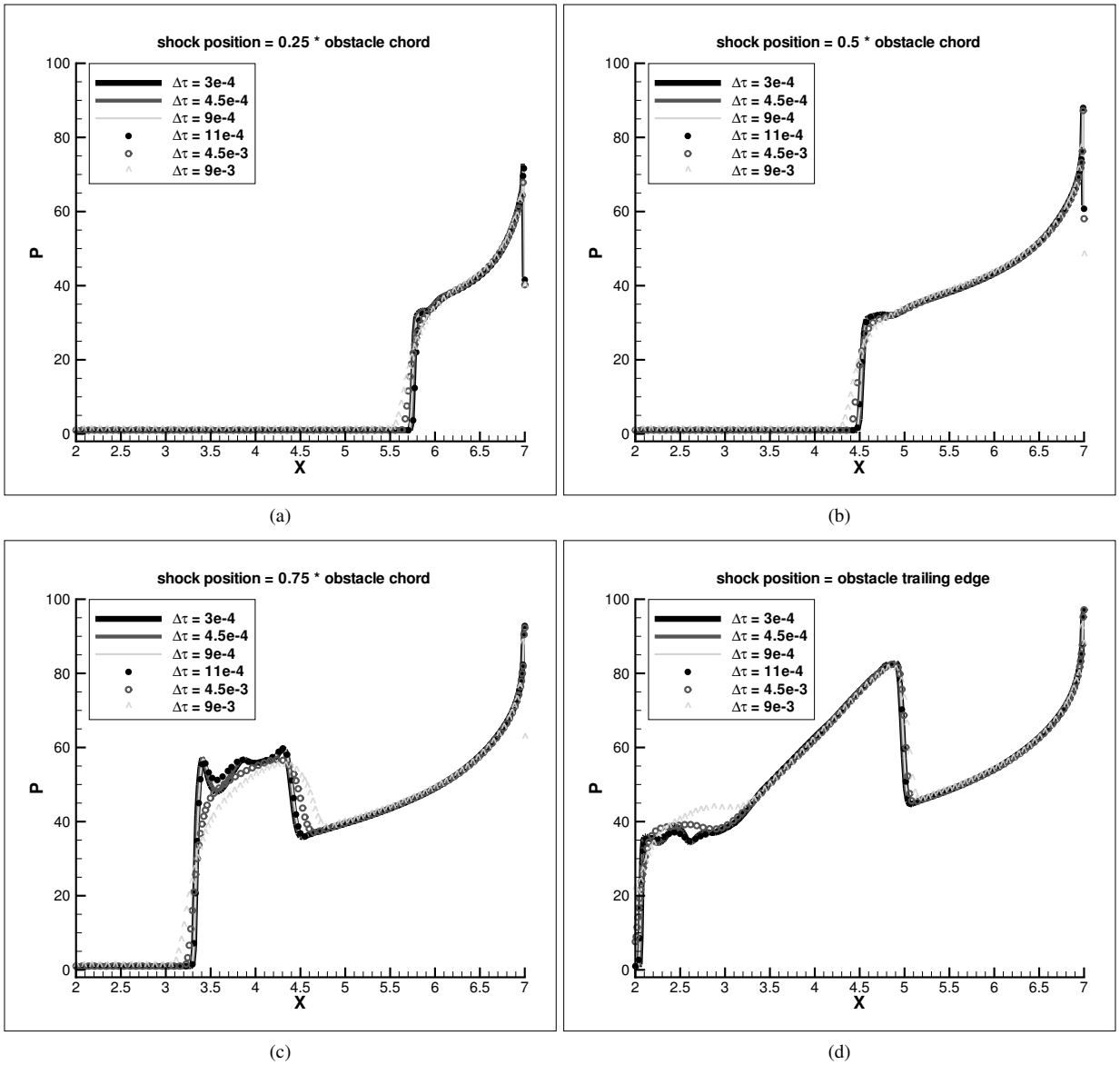

FIG. 4. Pressure—obtained with different time steps—on the obstacle during the propagation of a shock with Mach number of 4.7 at r_{LE}^{ref}, over a grid made of 56 000 nodes ($\Delta x = 0.01$). The shock advancement at each figure corresponds to 25% of the obstacle chord.

3. Assessment of the thermodynamic model

To describe the thermodynamic properties of air, the polytropic ideal gas model was adopted in the simulations. Air is a mixture of mostly diatomic gases, i.e. N_2 (78%) and O_2 (21%). In the experimental conditions of interest here, air is in the so-called dilute gas conditions and thermal properties are accurately predicted by the simple ideal mixture model of ideal gas.[26] Hence, the dimensional pressure $\widehat{\mathrm{P}}$ is $\widehat{\mathrm{P}} = R\widehat{\mathrm{T}}\widehat{\rho}$. $\widehat{\mathrm{P}}$ and $\widehat{\mathrm{T}}$ are made dimensionless with respect to the internal state pressure $\widehat{\mathrm{P}}_\mathrm{i} = 10^4$ Pa and temperature $\widehat{\mathrm{T}}_\mathrm{i} = 298.15$ K, respectively. The reference time is $L/(\widehat{\mathrm{T}}_\mathrm{i}R)^{1/2}$, where R is the mass averaged gas constant $R = \mathcal{R}/\sum_{h=1}^{n_c} M_h y_h$, with n_c the number of components of the gas mixture, M_h the molecular mass and y_h the molar fraction of the h-th component. For the considered air mixture, therefore, $R = 287.046$ J/(kg K).

A polytropic, i.e. constant specific heat, model is adopted for air up to the focusing of the shock wave. According to a-posteriori estimates, the maximum temperature of the flow is slightly lower than the lowest characteristic vibrational temperature of the air mixture, that is 2273 K (oxygen characteristic vibrational temperature) before shock focusing. Figure 6 reports the temperature distribution for the case producing the largest temperature value in the post-shock field ($N = 16$, $\beta_\mathrm{P} = 27$, $r_\mathrm{LE} = 14$ and $\ell/c = 0.07$). The dimensional value of the temperature is reported here, since it must be compared to the characteristic vibrational temperatures of the mixture. It can be observed that the temperature when the shock is approaching the focus point is still below the oxygen character-

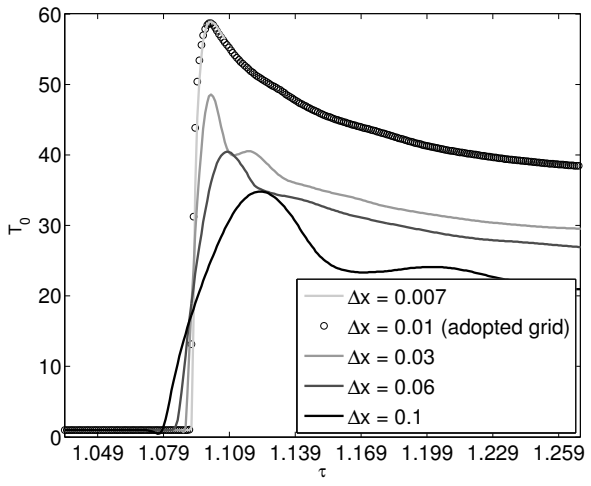

(a)Constant time step $\Delta\tau = 9 \times 10^{-4}$

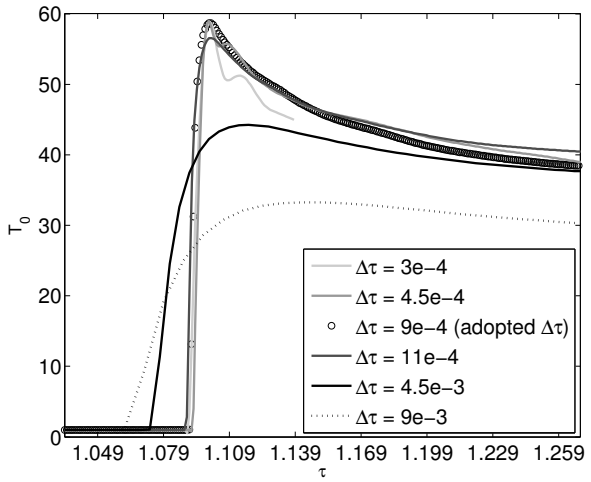

(b)Constant grid spacing $\Delta x = 0.01$

FIG. 5. Temperature value at the focus point versus time for different space (a) and time (b) discretizations.

istic vibrational temperature.

The perfect gas is a suitable model for predicting the shock propagation and reshaping, but it suffers from severe limitations in the simulation of the last part of the process, when the focusing takes place, because it cannot keep into account real-gas effects including ionization processes and the chemical reactions. Nevertheless, the maximum temperature values attained at the origin are qualitatively correlated to the average intensity of the shock evaluated in a region near the focus point but still in the region of validity of the constant-γ and thermo-chemical equilibrium assumption. The good agreement between the two sets of data—i.e. the temperature peak at the focus point and the shock intensity slightly before the focusing, respectively—suggests that, even if the simple thermodynamical model cannot capture the actual values of pressure and temperature at the focus point, it gives an indication on which configuration is more suitable to produce the most intense polygonal shock wave, and, therefore, the most effective focusing.

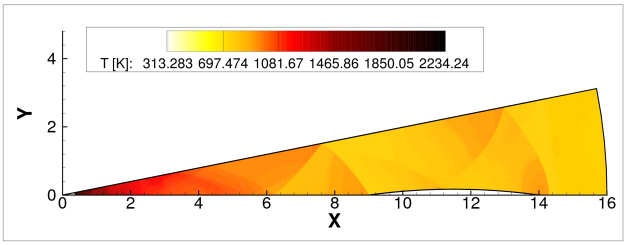

(a)

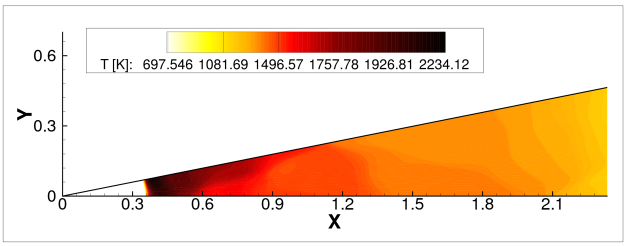

(b)

FIG. 6. (Colors online) Dimensional temperature distribution over the computational domain for the case producing the largest temperature value ($N = 16$, $\beta_P = 27$, $r_{LE} = 14$ and $t/c = 0.07$): (a) complete domain and (b) close up near the focus point. The maximum attained temperature in the flow field is indicated in the legend scale, i.e. 2234K, showing that, before the focusing, it remains below the oxygen characteristic vibrational temperature.

Real gas effects induced by high temperature are discussed also in, e.g., Ref. 27.

The assumption of a polytropic ideal gas is therefore verified to be valid here during all the convergence process, before the shock focusing.

4. Comparison with self-similar solutions and experimental results

The assessment of numerical results is provided amid the comparison with the self similar solution proposed by Guderley[16], which delivers the cylindrical shock radius R_s as a function of time τ as

$$\frac{R_s}{\tilde{r}} = \left(1 - \frac{\tau}{\tilde{\tau}}\right)^{\alpha} \tag{1}$$

where $\tilde{r}$ and $\tilde{\tau}$ are the initial shock radius and the total focusing time, respectively, and α is the self similarity exponent, whose value is computed in e.g. Ref. 16, 28–30 for different configurations.

The evaluation of the shock position is performed by means of a novel method based on Payne's, see also Ref. 17. The procedure developed by Payne[31] assumes the shock position R_s to be coincident with the point where the average pressure across the shock $P(R_s) = (P_b+P_f)/2$ is measured. The subscripts f and b indicate respectively in front and behind the shock. According to Ref. 19 and others, for one-dimensional isolated implosions with monotone trend of pressure P behind the shock, P_b and P_f are to be taken respectively as the maximum and

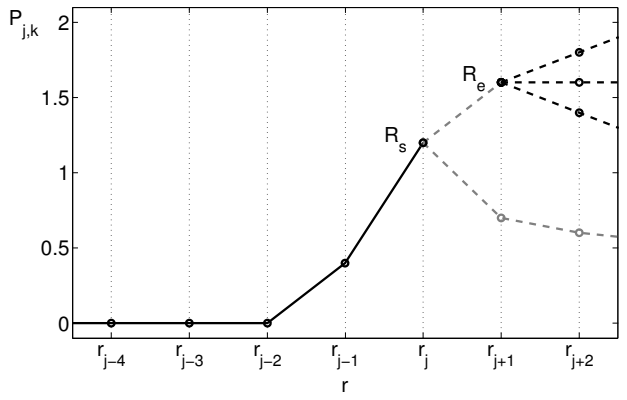

FIG. 7. Sketch of the expected discrete pressure profiles along the radius for given azimuth and time. Solid black lines represent the common part of the pressure distribution, dashed lines the various detectable trends.

minimum pressure values in the close proximity of the shock front. The modification proposed here accounts for the occurrence of post-shock waves, including contact discontinuities and rarefaction waves, and for the multidimensional nature of the flow field, whereas Payne considered only a single converging shock wave with cylindrical symmetry, followed at most by a monotonic expansion shock tail.

Along a given radial direction and at each time step τ_k—where k represents the time step index—a line of n_p equally distributed probes provides the pressure values $P_{j,k}$, with j the probes index, see fig. 7. The following first- and second-order differences are computed

$$d_r P_{j,k} = \frac{P_{j,k} - P_{j-1,k}}{r_j - r_{j-1}} \qquad j = 2, n_p \tag{2a}$$

$$d_r^2 P_{j,k} = \frac{P_{j+1,k} - 2P_{j,k} + P_{j-1,k}}{\left(r_j - r_{j-1}\right)^2} \qquad j = 2, n_p - 1 \tag{2b}$$

With reference to fig. 7, at each time step and for a given azimuth, a variety of pressure profiles can be encountered. The common features among these pressure distributions are that, for an ideal gas, the shock is always of compressive type and that the profile slope increases near the shock head. For a fixed azimuth, therefore, the shock location $R_s(\tau_k)$ is obtained as the minimum-radius probe j where all the following conditions are simultaneously satisfied

$$d_r P_{j,k} > 0 \qquad \text{(compression shock)} \tag{3a}$$

$$d_r^2 P_{j,k} \leq 0 \qquad \text{(inflection point or peak)} \tag{3b}$$

$$P_{j,k} - P_i > \epsilon \qquad \text{(numerical oscillation)} \tag{3c}$$

The use of first order backward finite differences (2a) is motivated by two possible pressure distributions along the ramp which approximates the numerical shock: it can either present an inflection point (upper gray dashed line in fig. 7) or it can have an increasing slope until a peak value is attained (lower gray dashed line in fig. 7). In the first case, the inflection point is assumed to represent the shock position because in most cases it is near the ramp midpoint; in the second one, the shock is assumed to be located in correspondence of the peak value. Both these configurations are captured by the conditions (3a) and (3b). The third condition is included to identify the numerical oscillations, which would cause the detection of false positives in correspondence of high-frequency pressure oscillations. It is therefore necessary to specify an additional condition on the value of $P_{j,k}$, i.e. (3c), which must differentiate from P_i by a threshold $\epsilon > 0$ which depends on the shock intensity. The average shock position at a given time step is finally obtained by averaging among the diverse shock positions detected at different azimuth.

In figure 8, the average radii of polygonal shocks are plotted versus time. The use of dimensional variables in fig. 8 allows to compare numerical results to experimental values obtained in Ref. 13. The shocks are generated by the reflection of cylindrical shocks with $M_s = 2.7$ over arrays of 6, 8, and 16 obstacles with $r_{LE} = 7$ and $t/c = 0.14$. Results for cylindrical shocks are reported for comparison. As demonstrated in Ref. 32, polygonal shocks exhibit a self-similar behavior and therefore a power law can be used to represent the data, provided that the so-called Schwendeman's conditions[32] are satisfied, namely, that the shock front has a regular polygonal shape. As discussed in sec. IV B 3, only in the reference case the reshaping is regular enough to satisfy Schwendeman's conditions. However, due to the high radial symmetry of the problem, it is still possible to apply a power law fit to the other configurations as well. Self-similarity exponents obtained with the fitting are 0.836 for the cylindrical shock (which is in good accordance with the theoretical value of 0.834), 0.879 for $N = 6$, 0.873 for $N = 8$ (which is in agreement to the reference value of 0.875 reported in Ref. 13) and 0.858 for $N = 16$.

Shock Mach numbers are compared with available experimental data[13] and are reported in figure 9. Similarly to figure 8, the shock radii are dimensional, to compare numerical results to experimental values. The average shock Mach number is computed as the ratio of the front speed s and the speed of sound in the unperturbed region c_i. The shock speed s is obtained by means of three methods. In the first approach, the shock speed is computed as the analytical derivative of the power law (PL). In the second one, s is obtained by means of centered finite differences (FD) of the shock position in time as follows

$$M_s^{PL}(\tau_k) = \frac{1}{c_i} \left.\frac{dR_s^{PL}}{d\tau}\right|_{\tau_k} \tag{4}$$

$$M_s^{FD}(\tau_k) = \frac{1}{c_i} \frac{R_s(\tau_{k+1}) - R_s(\tau_{k-1})}{\tau_{k+1} - \tau_{k-1}} \tag{5}$$

The last method moves from the mass conservation law across the shock front. In a reference frame moving at the flow velocity in the unperturbed state, from the Rankine-Hugoniot

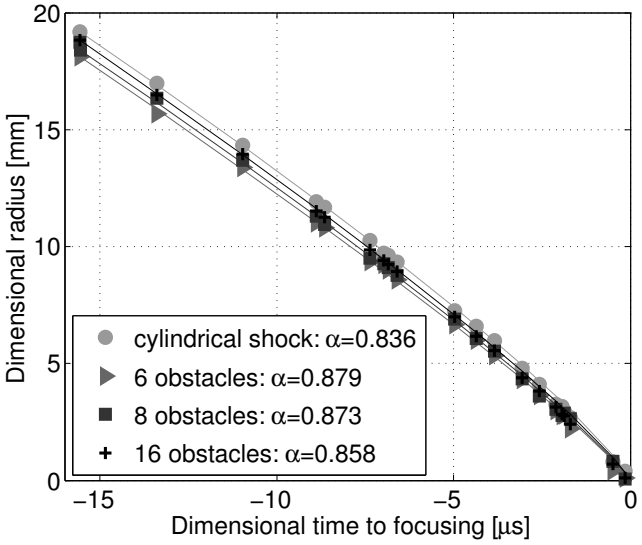

FIG. 8. Shock position versus time for cylindrical (●) and reshaped shocks obtained with arrays of 6 (▶), 8 (■), and 16 (+) obstacles. Power law fittings is shown in solid lines.

conditions one has

$$M_s^{RH}(\tau_k) = \frac{1}{c_i}\frac{\left|\vec{m}\left(R_e(\tau_k)\right)\right|}{\rho\left(R_e(\tau_k)\right) - \rho_i} \tag{6}$$

where $\vec{m}$ indicates the fluid momentum per unit mass. Subscripts i and e denote the internal and the external conditions of the imploding shock. Since the fluid is at rest ahead of the shock front, the above relation is valid in the laboratory reference as well.

The coordinate R_e is the radial coordinate of the first node immediately behind the shock. Note that in general $R_e \neq R_s$ since the shock front has a finite thickness due to numerical viscosity. Due to the presence of a non uniform, non monotone shock tail, the evaluation of R_e is not trivial. With reference to fig. 7, four possible configurations of shock tail can be observed. In the first configuration, represented by the lower gray line in fig. 7, the curvature of the shock profile is positive along the shock ramp and it assumes a negative value at $R_e \equiv R_s$. On the contrary, if the compression profile exhibits an inflection point (upper gray line in fig. 7), the pressure profile in the tail region can be either monotonically decreasing or increasing, or presents a local plateau.

In all the above situations, the curvature of the pressure profile assumes the largest value in the vicinity of point R_s. Therefore R_e is identified by the following conditions

$$\begin{aligned} &R_e \geq R_s \\ &d_r^2 P_{j,k} < 0 && \text{(negative concavity)} \\ &d_r^2 P_{j,k} \leq \min\left(d_r^2 P_{j+1,k},\ d_r^2 P_{j-1,k}\right) && \text{(largest curvature)} \end{aligned}$$

Results are reported in figure 9(a), where the three criteria are compared to the power-law fit. Notably, M_s^{FD} shows a reasonable agreement with the reference. Note that to reduce

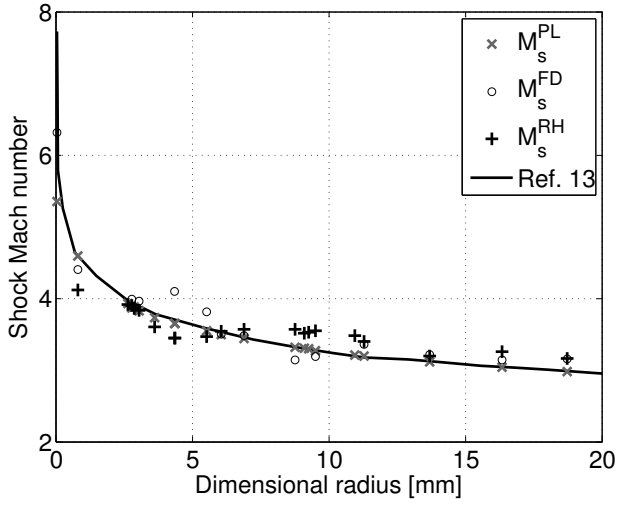

(a)

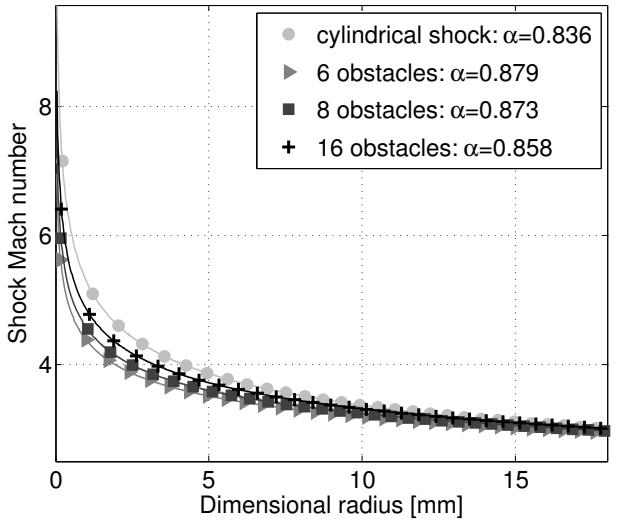

(b)

FIG. 9. (a) Shock Mach number at diverse radial positions calculated with diverse estimation methods for the shock speed. Analytical derivative of Guderley's law (×), centered finite differences (○), Rankine-Hugoniot relations (+). Reference value from Ref. 13 is in bold full line (—). (b) Mach numbers versus radius from fitting for diverse N for the reference M_s and geometry.

the dispersion in the numerical evaluation of the derivatives, only data set with a significant separation in time were considered. A large dispersion is observed for the so-called Rankine-Hugoniot method (6), which probably suffers from the high spatial variability of the quantities behind the reflected shock, in particular near the focusing.

A quantitative comparison is performed for the reference case ($N = 8, \psi_c = 0.14, r_{LE} = 7, M_s = 2.7$). In this case, it is possible to use the theory in Ref. 32 to compute the ratio between the Mach number $M_{s,n}$ of the polygon edges generated at the n-th reflection and $M_{s,n-1}$. Similarly to Ref. 13, the average shock Mach number between two consecutive reflections

	$M_{s,1}/M_{s,cyl}$	$M_{s,2}/M_{s,1}$	$M_{s,3}/M_{s,2}$
Theory (Ref. 32)	-	1.201	1.201
Experim. (Ref. 13)	N/A	1.20 ± 0.02	1.19 ± 0.03
Simul. (Present)	1.190	1.200	1.207

TABLE III. Ratios of the Mach numbers of shock edges generated between consecutive reflections. Theoretical predictions are from Ref. 32, experimental data from Ref. 13 and present numerical simulations.

is estimated by means of a stepwise linear regression on the shock radius. Theoretical,[32] experimental[13] and numerical results are reported in table III for three reflections. A very good agreement is found for the reference configuration. Note that in the first reflection, the incident shock front is cylindrical and therefore the theory is not applicable.

IV. SHOCK WAVE INTERACTION WITH OBSTACLE ARRAYS

Results of numerical simulations are reported in this section. In the first part, the values of pressure and temperature peaks attained at the focus point are reported. In section IV B, the shock reflection patterns are described.

A. Maximum pressure and temperature at the focus point

The most relevant quantities in shock focusing are the maximum values of the compression and temperature factors attained at the focus point. The compression factor and the temperature factor are defined as

$$c_P = \frac{P_0^M(k)}{P_i} \tag{8a}$$

$$c_T = \frac{T_0^M(k)}{T_i} \tag{8b}$$

where $P_0^M(k)$ and $T_0^M(k)$ are respectively the minimum-time pressure and temperature values in the origin such that

$$P_0^M(k) \geq \max\left(P_0(k+1), P_0(k-1)\right) \tag{9a}$$

$$T_0^M(k) \geq \max\left(T_0(k+1), T_0(k-1)\right) \tag{9b}$$

The condition on the minimum time is introduced because of the complex flow structure behind the reshaped shock, where several reflected waves are present, see fig. 5. However, only the P and T peak values due to the main shock are relevant for applications.

Figure 10 reports c_P (a) and c_T (b) at the origin as functions of the shock Mach number M_s at r_{LE}^{ref}, as well as the obstacles aspect ratio. The curves are parametrized by the number of obstacles. The shock Mach number at the impingement is considerably more influential than the number of obstacles,

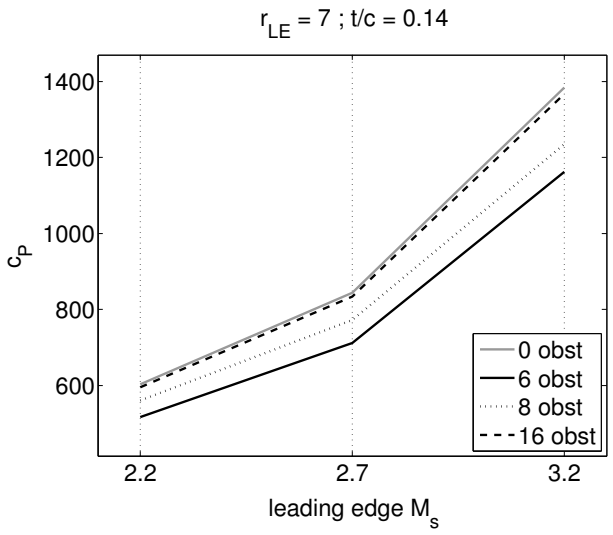

(a)

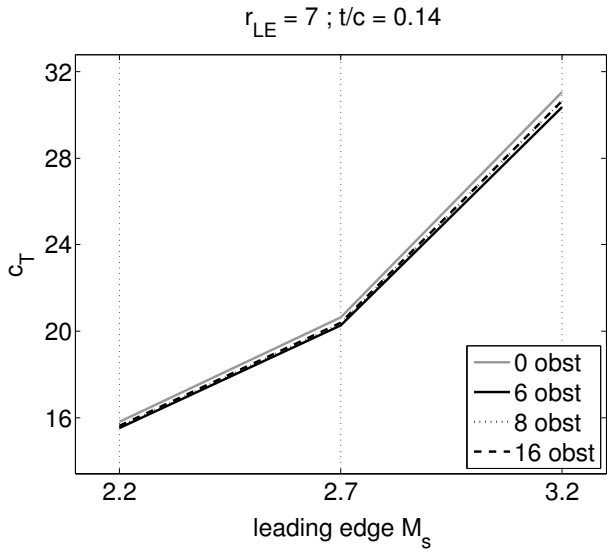

(b)

FIG. 10. Maximum pressure (a) and temperature (b) attained at the origin after a reshaping obtained by means of obstacles with reference aspect ratio.

for reference obstacle shape and position. Moreover, the attained pressure peak presents in general a non monotone trend with respect to the number of obstacles.

Figures 11 and 12 report the same quantities, but for higher and lower t/c values, respectively. For both types of obstacles the monotone increasing trend is preserved with respect to the shock Mach number.

Figs. 10 to 12 illustrate also the envelope of the curves for the temperature factor. A non monotone dependence is observed on the number of obstacles. Therefore, a further analysis is performed on the blockage effect of the obstacles, simulating cases with diverse number of obstacles. The correlation between the peak pressure and temperature and the number of obstacles, parametrized by the initial Mach number, is re-

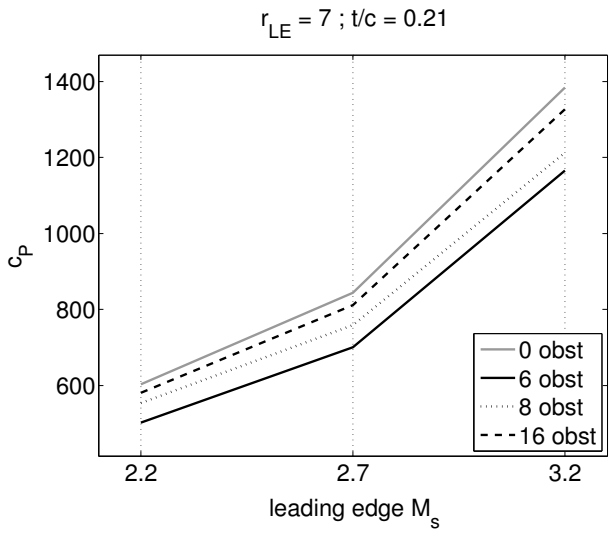

(a)

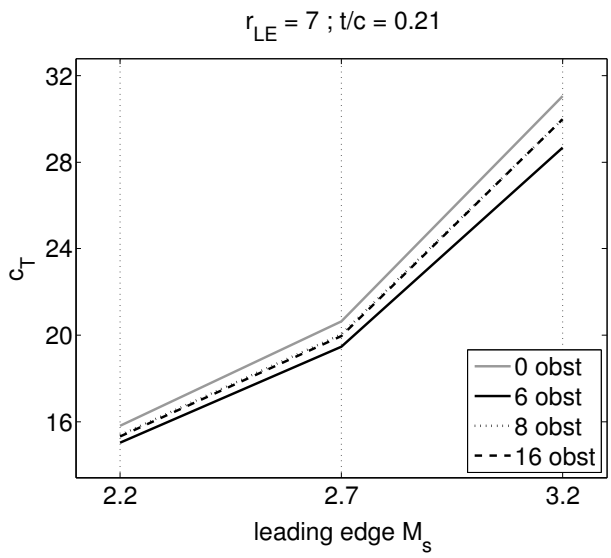

(b)

FIG. 11. Maximum pressure (a) and temperature (b) attained at the origin after a reshaping obtained by means of obstacles with thickness-to-chord ratio of 0.21, corresponding to 150% of the reference value.

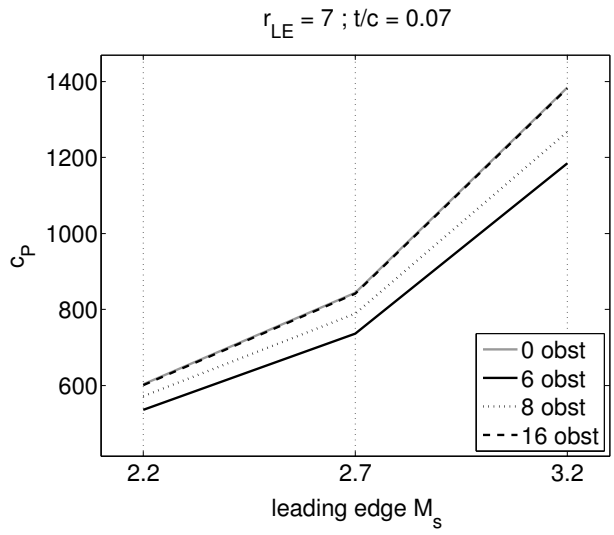

(a)

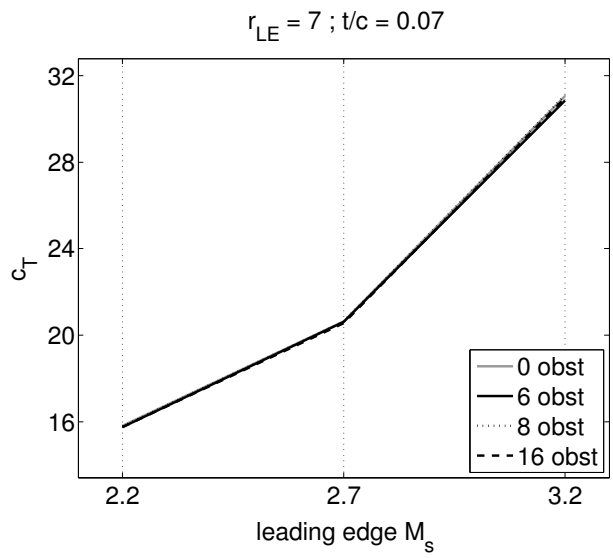

(b)

FIG. 12. Maximum pressure (a) and temperature (b) attained at the origin after a reshaping obtained by means of obstacles with thickness-to-chord ratio of 0.07, corresponding to 50% of the reference value.

ported in figure 13. Also in this case, the number of obstacles is found to be a relevant parameter influencing the peak value of the temperature.

The effects of the obstacle position and aspect ratio are reported in figure 14: even for diverse combinations of M_s and number of obstacles, the highest temperature values are obtained for obstacle with thickness-to-chord ratio of 0.07, with no relevant exceptions. The temperature dependence on the leading edge radius is generally non-monotone.

According to the present simulations, the configuration producing the highest temperature at the focus point is the combination of sixteen obstacles with $t/c = 0.07$ located at twice the reference distance and overrun by a shock generated by an initial pressure ratio of 27. For this case, the temperature peak interval, defined as the time interval along which the temperature remains within the 90% of the maximum value, is approximately $\Delta\tau/\bar{\tau} = 0.013$. It is remarkable that this new configuration delivers a focus efficiency—defined as c_P/β_P—that is only slightly better (2-3%) than the reference one at the same Mach number, thus confirming the goodness of the obstacle arrangement proposed in Ref. 13.

The trade off between effectiveness (large c_P and c_T) and efficiency (c_P/β_P) of energy focusing is confirmed also by a more general analysis on a larger range of M_s. Figure 15, indeed, reports the correlation between the initial pressure ratio β_P and the Mach number of the shock wave when it is about to be

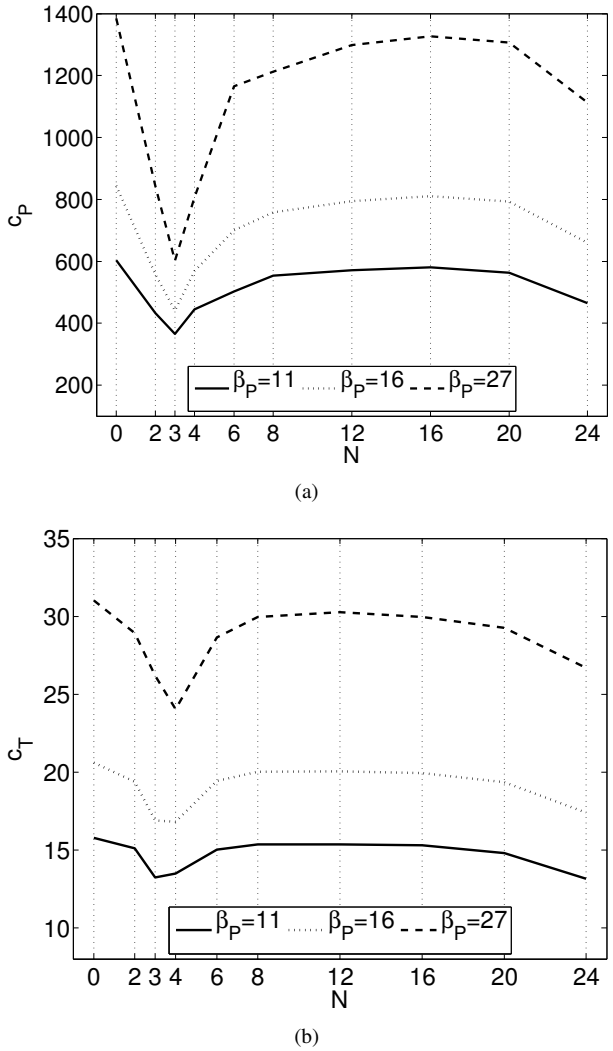

FIG. 13. (a) Pressure and (b) temperature at the origin as functions of the number of obstacles, parametrized by the initial Mach number, for obstacles with $t/c = 0.21$.

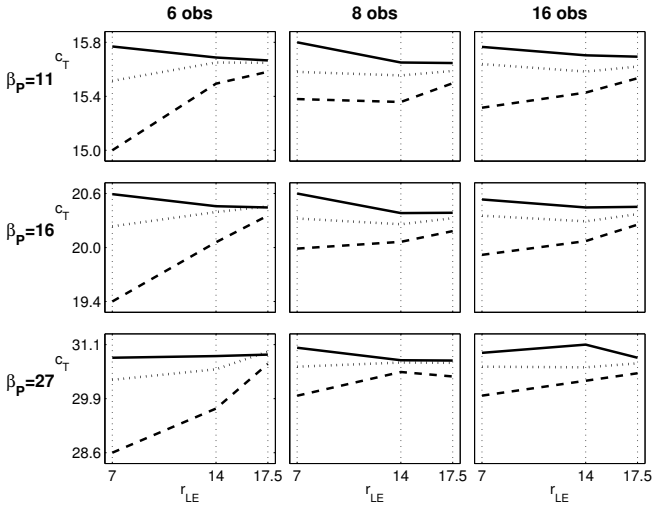

FIG. 14. Maximum temperature value attained at the focus point for reference shaped obstacles versus leading edge radius for diverse M_s and N, parametrized by the obstacle thickness-to-chord ratio: 0.07 (full line), 0.14 (dotted line), 0.21 (dashed line).

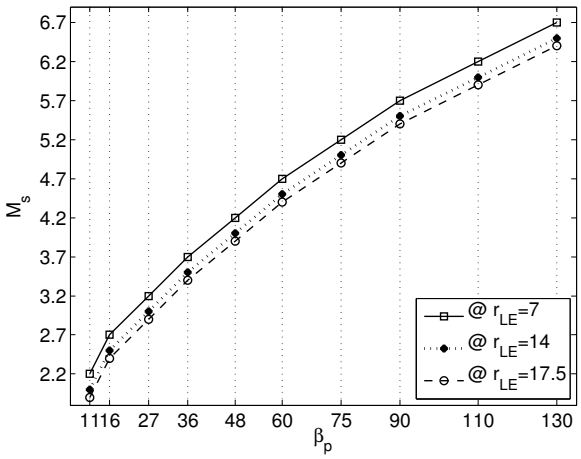

FIG. 15. Correlation between the initial pressure ratio and the Mach number of the shock wave when it is about to be diffracted by the obstacle leading edge, for diverse r_{LE} values.

diffracted by the obstacle leading edge. It shows that, regardless of the considered r_{LE}, M_s grows less-than-linearly with respect to β_P, and therefore the shock efficiency decreases with M_s.

B. Shock reflection patterns

Shock reflection patterns are described in this section. In sec. IV B 1, leading-edge reflection types are assessed for diverse values of the leading-edge wedge angle and incident shock Mach number. Sec. IV B 3, describes the pseudo-polygonal shocks resulting from the reshaping, highlighting the possible formation of shocks with more edges than the theoretical expected value of N and $2N$. The features of the reflections occurring downstream the leading edge are the topic of the following three sections. In particular, the reflection of wave A over the upper symmetry boundary is discussed in sec. IV B 4, the effect of the obstacle concavity on the interaction of the multiple-waves systems is presented in sec. IV B 5 and the overall number of reflections of the shock before its focusing is reported in sec. IV B 6. Eventually, section IV B 2 describes the trajectory of the first Triple Point (leading-edge triple point).

1. Leading edge reflections

The types of leading edges reflections are compared with those predicted by the theory of Ben-Dor et al.[15], which combines the effects of the flow deflection caused by a sharp wedge (with semi-opening angle θ_w) and the two and three-

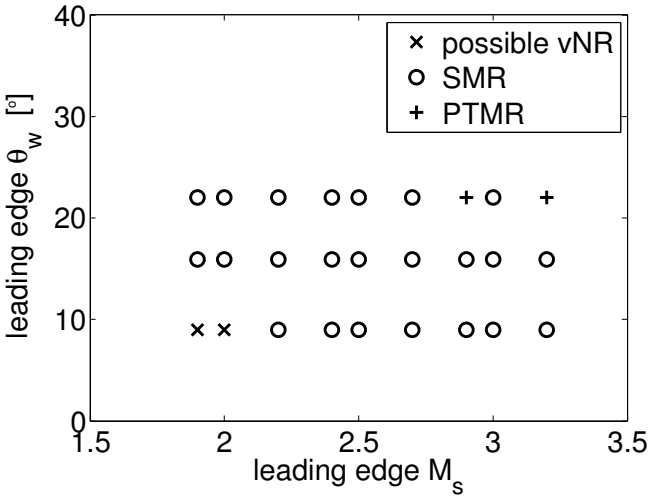

FIG. 16. Obstacle leading edge reflections occurring for given combinations of local M_s and θ_w: pseudo-transition Mach reflections (PTMR), single Mach reflections (SMR) and possible von Neumann reflection (vNR).

shock theories. This model is derived for the diffraction of planar shocks by straight wedges, which exhibit a pseudo-steady behavior. Applicability to the present numerical results is limited by the non uniform distribution of Mach number behind the shock, the curvature of the obstacle borders and the global unsteadiness. Therefore, only local values of M_s and θ_w are used for the reflection pattern assessment, and only qualitative considerations are drawn. The possibility of using pseudo-steady models as a reference in the observation of unsteady reflections is discussed also in Reference 33.

Figure 16 compares the reflections detected in correspondence of the obstacle leading edge with the transition boundaries predicted by the shock diffraction theory for straight shocks and wedges.

The accordance is fairly good, except for the case with the obstacles located at twice the reference distance and with the highest shock Mach number and t/c. In these conditions, a single Mach reflection (SMR) is observed instead of a Pseudo-Transitional Mach Reflection (PTMR). It is however worth noticing that this is the case where both the shock and the wedge curvatures are most relevant, and therefore it is the case where the observed configuration differs most from the theoretical model.

In accordance with Ref. 34, an irregular reflection is detected at the leading edges of thin obstacles. As reported in figure 17, for certain values of M_s, either a classic SMR or a von Neumann reflection (vNR)[35] may occur, depending on θ_w. In figure 17(a), a smooth transition from the incident shock to the Mach stem and the compression of wave A is observed. This flow structure is referred to as an equivalent triple point in the literature. In 17(b), instead, a genuine triple point is apparent.

Due to the small curvature of the Mach stem near the triple point, the transition between the two types of irregular reflection is not evident. In accordance to pseudo-steady models

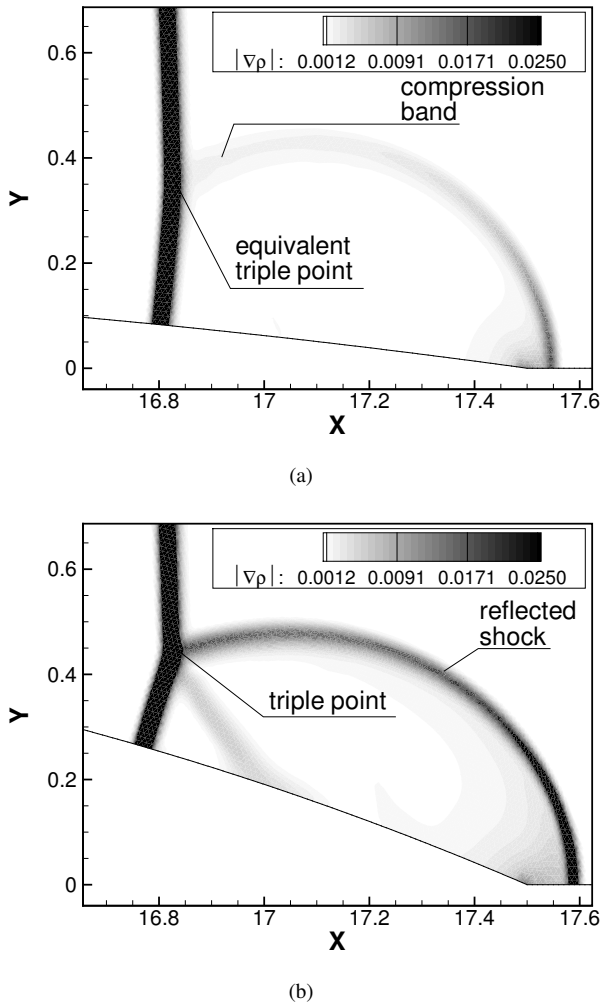

FIG. 17. (a) possible vNR and (b) SMR at the leading edge of higher and lower obstacle thickness ($\beta_P = 11$).

described in Ref. 15 the two reflection types can be separated by evaluating the local value of the angle between wave A and the streamlines behind the incident shock in a coordinate system attached to the triple point. This observation suggests the occurrence of a vNR in reflections of shocks generated by the lowest initial blowup ($\beta_P = 11$) over obstacle at distances such that the local M_s is lower than 2 (that is $r_{LE}/r_{LE}^{ref} = 2$ and 2.5). It is however to be noticed that, in absence of higher spatial resolution, it is impossible to guarantee that the aforementioned reflection is of vNR rather than SMR type.

2. *Triple point trajectory*

Figure 18 reports the trajectories of the leading edge triple point until the secondary reflection for diverse obstacle configurations and different values of the initial pressure ratio β_P.

The obstacle curvature is found to influence the trajectory shape, deviating it from the straight line predicted for pseudo-steady reflections by Law and Glass[36] and by more sophisti-

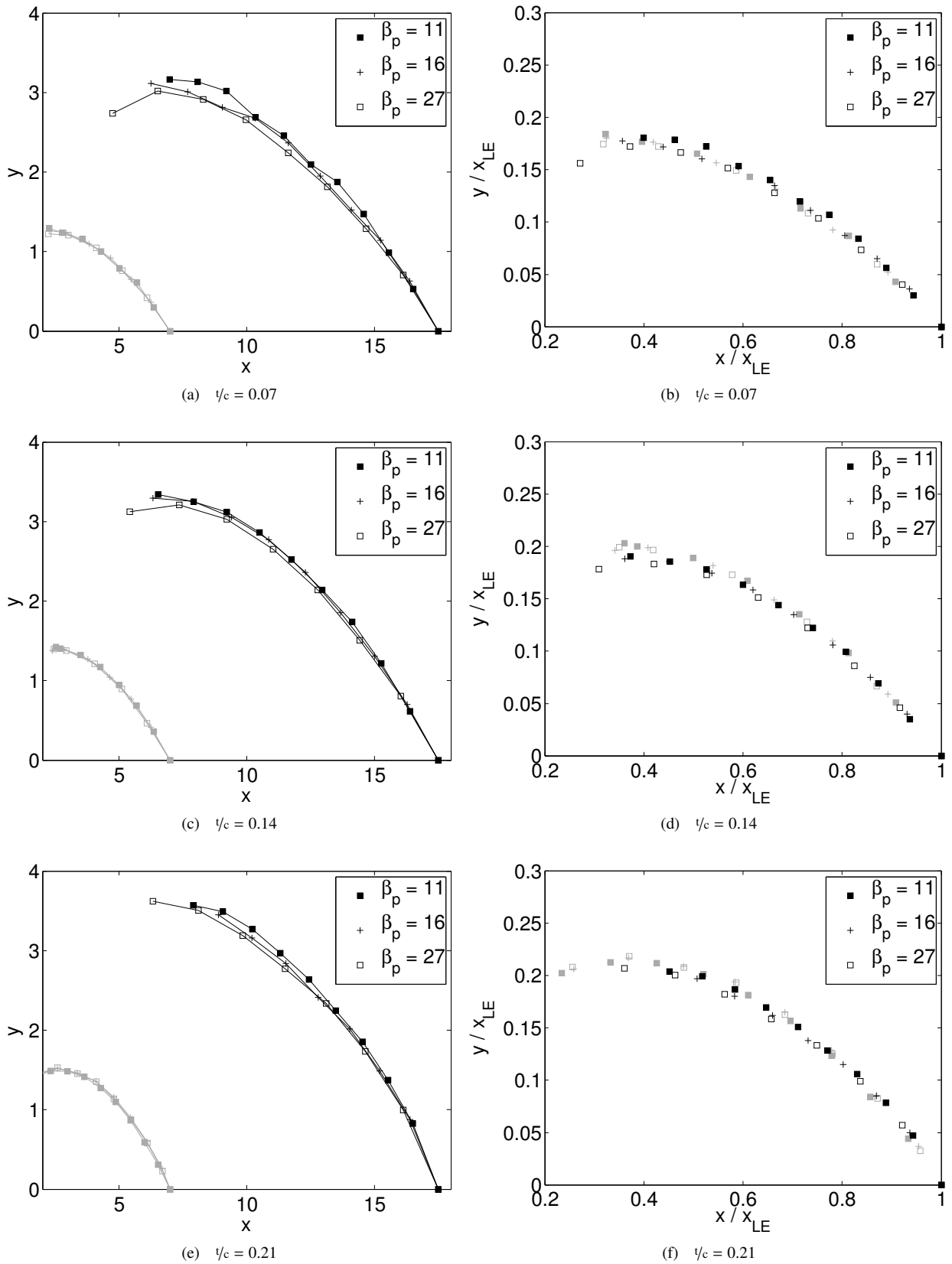

(a) $t/c = 0.07$ (b) $t/c = 0.07$

(c) $t/c = 0.14$ (d) $t/c = 0.14$

(e) $t/c = 0.21$ (f) $t/c = 0.21$

FIG. 18. Trajectories of the triple point generated at the leading edge for (a) thin, (c) reference and (e) thick obstacles for diverse initial pressure ratios and obstacle leading edge radii (● for $r_{LE} = 7$, ● for $r_{LE} = 17.5$).

cated non-self similar theories.[37] The wave Mach number M_s has a negligible influence on the trajectory shape.

The radius of curvature of the trajectory is observed to be proportional to r_{LE}, which is found to be the most significant parameter among the considered ones. In figures 18(a)-(c)-(e), different behaviors are identified between the black groups of curves (r_{LE} = 17.5) and the gray ones (r_{LE} = 7). On the contrary, when the coordinates of the triple point trajectories are normalized with r_{LE}, these curves gather together (figs. 18(b)-18(d)-18(f)). It is worth noticing that the trajectory of the triple point presents high dispersion for thin obstacles, due to the impending transition of the leading edge reflection from SMR- to vNR-type, for which the definition of the triple point is ambiguous.

3. Shock reshaping process

Past the leading edge reflection, that is the first step in accordance to the nomenclature in section II, diverse patterns can be identified depending on the obstacle arrangement and geometry.

Indeed, the shock reshaping process described in section II, where four distinct steps take place and the final shock consists of a regular polygonal front, is not the most recurrent, since it occurs only for peculiar combinations of the shock speed and the geometry. More frequent is the occurrence of further intermediate reflections, which cause a distortion of the reshaped polygon and hence modify the effectiveness of the shock wave. As an example, figure 19 illustrates the numerical Schlieren of the solution on an elementary domain and the reconstructed polygonal shock on the basis of symmetry considerations. Dashed lines and circles represent the polygon edges and vertexes, respectively. The sequence of pictures in figure 19, therefore, depict a sudden switch from a $3N$ polygonal shock (a) to N one (b) at the conclusion of the step 3. The following reflection occurring downstream the obstacle causes the onset of a shock in correspondence of the trailing edge, as well as a Mach stem which increases the number of edges from N (b) to $2N$ (c). The evolution of the latter reflection results in a "reshaping cascade", which produces a continuous transformation of the shock from a N-edge to a $2N$-edge to a N-edge again, even though rotated (d), and so on. The "reshaping cascade" was predicted by Schwendeman et al.[32], who demonstrated the onset of a continuous N-$2N$ transition until the focusing, and experimentally verified in Ref. 13. As experimentally confirmed also in Ref. 38 for cylindrical obstacles, the onset of the transition is related to the type of reflection (regular or Mach-type) occurring in correspondence of symmetry surfaces. It is worth noticing that the aforementioned Direct Mach Reflection causes the Mach stems to present a slight curvature. In fig. 19(b) it is apparent that the edges of the 8-sides polygon representing the shock are curved. Therefore the numerical secondary Mach stem and the approximating polygon side differ significantly. However, the absence of additional reflections of the secondary Mach stem over the symmetry surface preserve the shock topology and no additional vertexes are introduced to describe it.

The present numerical simulations show that the phenomenon can become much more complex and may possibly include $3N$ and $4N$ configurations. Indeed, reflections occurring downstream the obstacle satisfying conditions in Ref. 32 are not the only cause for departure from the regular polygonal shock shape. For instance, if the trailing edge is not located along the trajectory of the secondary triple point, that is the first Mach stem reaches the obstacles trailing edge before the conclusion of the shock reshaping, the non orthogonality between the first Mach stem and the symmetry line causes a further reflection: in this case, if the latter reflection is of Mach type, the number of edges, in addition to the aforementioned N and $2N$, becomes $3N$ and $4N$ (figure 20).

4. Secondary reflection

The secondary reflection, taking place on the upper symmetry lines during the second reshaping step, involves the reflection of two waves. The first one, the Mach stem generated by the leading edge reflection, undergoes an MR. This is in accordance with the three-shock theory, which now fully applies, since the reflecting surface is straight and the incident shock is a pseudo-straight wave moving at approximately constant speed. The second shock which is reflected on the symmetry surface is wave A, which undergoes either an RR or an MR (figure 21).

With reference to table IV, MR are usually observed in correspondence of larger obstacle numbers and thickness. For a given set of parameters, in fact, the *perceived wedge angle* θ_w^P—i.e. the angle of the diffracting wall perceived by wave A at its reflection over the upper symmetry surface—is lower for a larger number of obstacles, as sketched in figure 21. Moreover, the higher is the obstacle thickness, the stronger is the curvature of wave A, which contributes to reducing the value of the equivalent θ_w^P too. Therefore, the most relevant parameters influencing the secondary reflection type are N and t/c.

For a given configuration, the type of secondary reflection seems not to significantly influence the following reflection patterns.

5. Trailing edge reflections dynamics

The obstacle arrangement strongly influences the dynamics of the reflections after the shock reaches the obstacle trailing edge. In particular, the obstacle thickness and position are observed to influence the curvature of wave A (cf. section II) and the triple point trajectory, and therefore to condition also the following reflections.

Figures 22 and 24 depict the reshaping of an exemplary cylindrical shock generated by an initial pressure step $\beta_P = 11$ for two configurations, namely (N = 8, t/c = 0.21, r_{LE} = 14) and (N = 6, t/c = 0.21, r_{LE} = 7), respectively. The diverse obstacle arrangements cause the onset of different shock patterns.

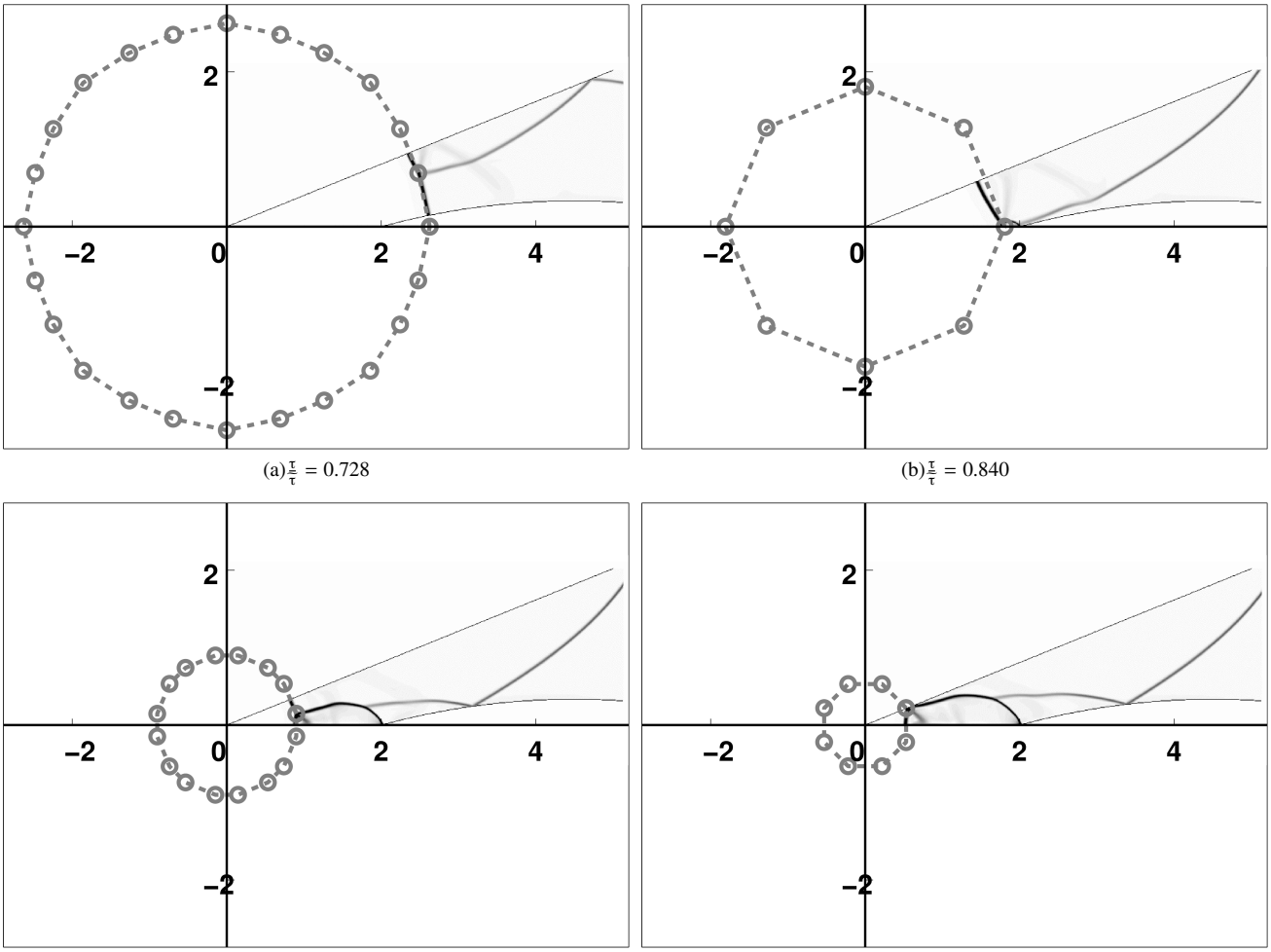

FIG. 19. Numerical Schlieren of the shock reshaping process in reference conditions, showing the reshaping cascade. The 2π polygonal shape is reconstructed from the numerical simulations carried out in the elementary $\pi/8$ subdomain. (a) During step 3, the number of edges is three times the number of obstacles. (b) The number of edges equals the number of obstacles, vertices are along symmetry lines crossing the trailing edges. (c) The number of edges is twice the number of obstacles. (d) The number of edges equals the number of obstacles, vertices are aligned with other symmetry lines. The indicated time advancement is computed from the shock impingement over the obstacle leading edge till the focusing.

In sec. II, the reference configurations was shown to produce a relatively simple pattern: the reshaped polygonal shock has a number of edges switching from N to $2N$ and back during the shock propagation, see figure 19. In fig. 22, a more complex case is represented. The leading edge Mach reflection of the cylindrical shock results in the three-shock structure consisting of the incident shock i_s, of the reflected wave A (defined in sec. II) and of the leading edge Mach stem m_{LE} (fig. 22(a)). This peculiar configuration is well known from previous theoretical, numerical and experimental studies on shock reflection, see e.g. Ref. 15. When the shock reaches the trailing edge, m_{LE} is diffracted into the trailing edge Mach stem m_{TE} and into wave C, which intersect at the trailing edge triple point TP_{TE} (fig. 22(b)). Afterwards, the secondary reflection of the first, leading-edge triple point over the upper symmetry line occurs (cf. figure 2), resulting in the onset of wave B and of the secondary Mach stem m_{sec} (fig. 22(c)). Eventually (fig. 22(d)), a head-on collision between waves B and C occurs; the resulting shocks then interacts with the upper and lower symmetry lines. Because of the comparable intensity and size of waves B and C, a symmetric reflection system is observed. The sequence of the reflections of waves B and C over the upper and lower symmetry lines is denoted by waves B', B", etc. and C', C", etc. respectively, as illustrated in fig. 23.

In fig. 24, a small variation in the obstacle arrangement is seen to cause a significantly different final pattern, thus pointing to the highly non-linear nature of the problem. Indeed, in fig 24(a), the leading edge reflection is a SMR as in the previous case (cf. fig. 22(a)). In the present configuration, wave A reaches the upper symmetry line while the shock is still crossing the obstacle (fig. 24(b), to be confronted with fig. 22(b)), and wave B is generated. Wave C is generated at the trailing edge reflection of m_{LE} (fig. 24(c)) as in the previ-

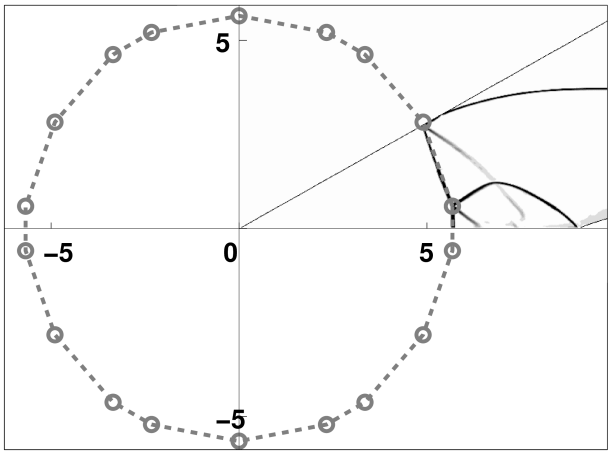

(a) $\frac{\tau}{\tau^*} = 0.665$

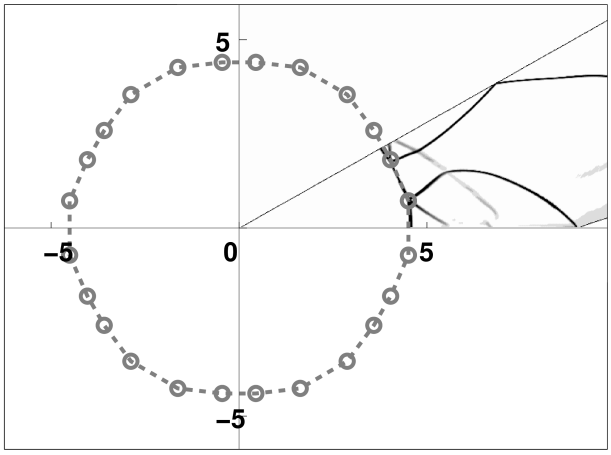

(b) $\frac{\tau}{\tau^*} = 0.743$

FIG. 20. Numerical Schlieren after the interaction with 6 obstacles of $t/c = 0.21$ at twice the reference distance ($r_{LE} = 14$) and initial pressure ratio of 27. The shock becomes (a) an optadecagon ($3N$) and (b) an icosikaitetragon ($4N$). The deviation of the reflected wave from the classical SMR shape is due to the interaction with contact discontinuities generated during previous reflections, and it is not due to an actual TMR. The indicated time advancement is computed from the shock impingement over the obstacle leading edge till the focusing.

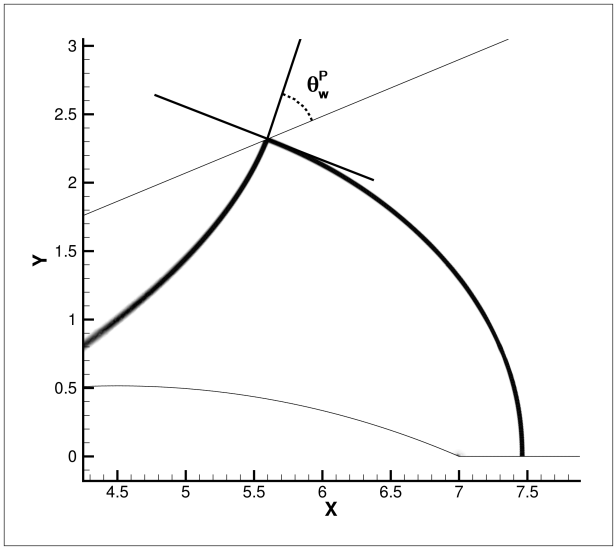

(a)

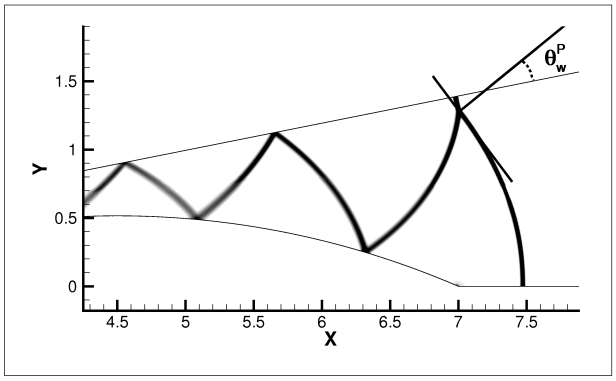

(b)

FIG. 21. Numerical Schlieren of the secondary reflection caused by thick obstacles at reference distance ($\beta_P = 16$): (a) regular (8 obstacles) and (b) Mach type (16 obstacles) caused by diverse values of the angle of the diffracting corner perceived by wave A, thus the perceived wedge angle θ_w^P.

ous case. Its interaction with waves B takes place when wave C is still a small-amplitude shock. As a result, wave B is only slightly affected by the interaction with wave C and eventually reflects into wave B' over the lower symmetry boundary. The reflected wave B' propagates towards the upper symmetry line and coalesce with wave C (fig. 24(d)). From this moment, one complex wave hereafter termed *multiple wave*, consisting of the overlapping of waves B' and C, is observed (fig. 25).

The diverse interactions between the reflected waves downstream the trailing edge result in polygonal shocks with variable edge numbers and intensity and, in general, in a more complex flow field with respect to the reference configuration in Ref. 13. Indeed, the presence of several single waves rather than one multiple wave causes further reflections. Fig. 26(a) details the flow field near the trailing edge for the first case described in this section ($N = 6$, $t/c = 0.21$, $r_{LE} = 7$, $\beta_P = 11$) at an intermediate time between those depicted in figs. 22(d) and 23: it is apparent that wave C reaches the symmetry surface before the triple point, and undergoes two regular reflections. On the contrary, the above is not observed in figure 26(b) ($N = 6$, $t/c = 0.21$, $r_{LE} = 14$, $\beta_P = 11$, intermediate time between 24(d) and 25), where the triple point reaches the reflecting surface first. Therefore, the above interaction sequence is chosen as the criterion to distinguish the two reflection pattern.

Numerical simulations reveals that a larger obstacle distance and thickness cause the reflected wave to approach the symmetry surface before the triple point, as illustrated in table V, thus resulting in the reflection pattern described in fig. 26(a). Obstacles with larger thickness, indeed, generate reflected shocks (wave A) with larger curvature, which extend more significantly towards the upper symmetry line. As

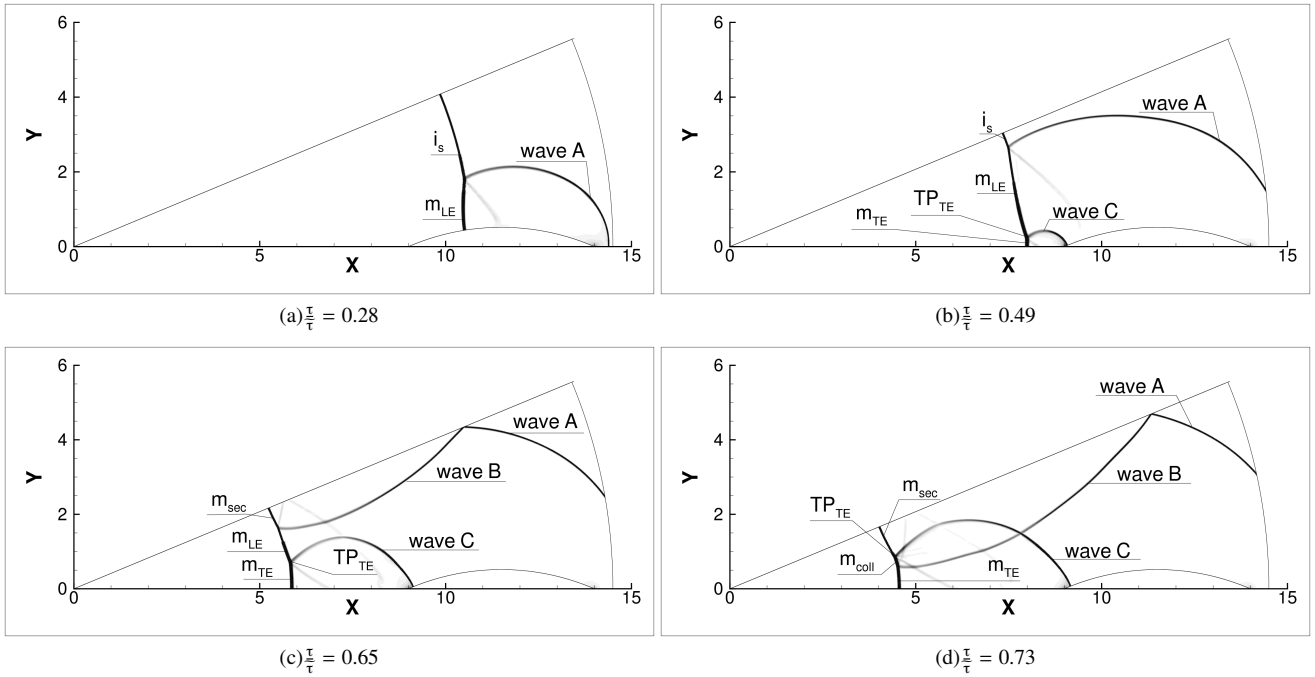

(a)$\frac{\tau}{\bar{\tau}} = 0.28$ (b)$\frac{\tau}{\bar{\tau}} = 0.49$

(c)$\frac{\tau}{\bar{\tau}} = 0.65$ (d)$\frac{\tau}{\bar{\tau}} = 0.73$

FIG. 22. Numerical Schlieren images representing the reshaping of a shock generated by an initial pressure ratio $\beta_P = 11$ over an array of 8 obstacles with $r_{LE} = 14$ and $t/c = 0.21$. (a) Mach reflection of the incident shock i_s and formation of the leading edge Mach stem m_{LE} and of wave A. (b) Mach reflection of m_{LE} at the trailing edge and formation of the trailing edge Mach stem m_{TE} and of wave C, merging at the triple point TP_{TE} (c) Secondary reflection over the upper symmetry line, resulting in the onset of wave B and of the secondary Mach stem m_{sec} (d) Head-on collision of waves B and C, resulting in a weak distortion of the two waves and in the formation of the collision Mach stem m_{coll} (The indicated time advancement is computed from the shock impingement over the obstacle leading edge till the focusing).

TABLE IV. Secondary reflection type: MR are concentrated in the top-right part of each block, corresponding to higher t/c and N.

	r_{LE}	7			14			17.5		
β_P	N \ t/c	0.07	0.14	0.21	0.07	0.14	0.21	0.07	0.14	0.21
11	24			MR	MR	MR	MR			
	16	?R	RR	MR	?R	RR	MR	?R	MR	MR
	8	?R	RR	RR	?R	RR	RR	?R	RR	RR
	6	?R	RR	RR	?R	RR	RR	?R	RR	RR
16	24			MR	MR	MR	MR			
	16	RR	RR	MR	RR	RR	MR	RR	MR	MR
	8	RR	RR	RR	RR	RR	RR	RR	RR	RR
	6	RR	RR	RR	RR	RR	RR	RR	RR	RR
27	24			MR	MR	MR	MR			
	16	RR	RR	MR	RR	RR	MR	RR	MR	MR
	8	RR	RR	RR	RR	RR	RR	RR	RR	RR
	6	RR	RR	RR	RR	RR	RR	RR	RR	RR

a consequence, for thick obstacles the reflected shock waves reaches the symmetry line before the triple point, as in figure 26(a).

The effect of the parameter r_{LE} on the shape of the trailing edge reflection is indirect. Indeed, wave C always interacts with wave B before reflecting at the upper symmetry line.

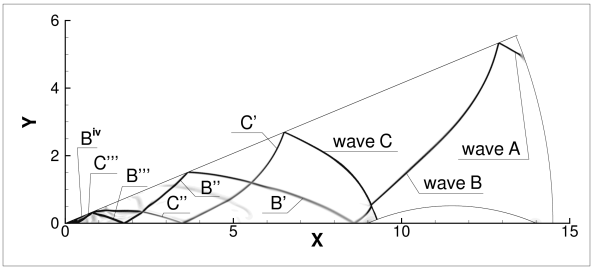

FIG. 23. Evolution of the reflections of waves B and C, which remain independent waves almost until the shock focusing ($N = 8$, $t/c = 0.21$, $r_{LE} = 14$, $\beta_P = 11$, $\frac{\tau}{\bar{\tau}} = 0.87$).

Hence, the stronger wave B is, the more significant is the deformation of the trailing-edge reflected wave resulting from their interaction (as it is evident in fig. 26(b)). Therefore, the trailing-edge triple point TP_{TE} is more likely to reach the reflecting surface before wave C. In this respect, the effect of r_{LE} on the intensity of wave B is twofold. On one hand, for a given β_P, a larger r_{LE} implies a lower shock Mach number M_s of the incident shock, resulting in a weaker leading edge reflection. As a consequence, wave B is less intense as well. Moreover, the larger is r_{LE} (for a given N), the longer is the distance between the obstacle leading edge and the upper reflecting surface. Therefore a stronger attenuation of wave A is observed as it diffracts from the leading edge. Note that

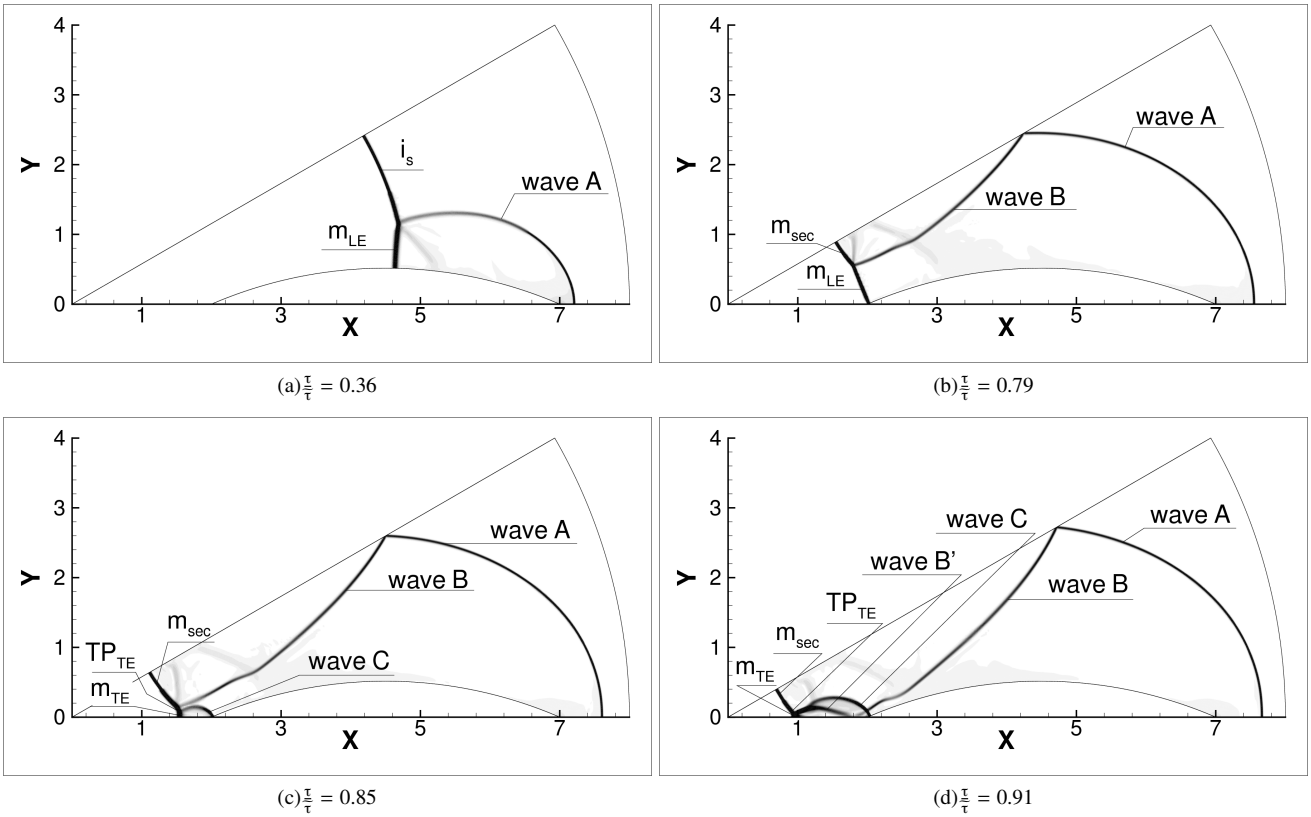

(a)$\frac{\tau}{\bar{\tau}} = 0.36$ (b)$\frac{\tau}{\bar{\tau}} = 0.79$

(c)$\frac{\tau}{\bar{\tau}} = 0.85$ (d)$\frac{\tau}{\bar{\tau}} = 0.91$

FIG. 24. Numerical Schlieren images representing the reshaping of a shock generated by an initial pressure ratio $\beta_P = 11$ over an array of 6 obstacles with $r_{LE} = 7$ and $t/c = 0.21$. (a) Mach reflection of the incident shock i_s and formation of the leading edge Mach stem m_{LE} and of wave A. (b) Secondary reflection over the upper symmetry line, resulting in the onset of wave B and of the secondary Mach stem m_{sec} (c) Mach reflection of m_{LE} at the trailing edge and formation of the trailing edge Mach stem m_{TE} and of wave C, merging at the triple point TP_{TE} (d) Coalescence of waves C and B' (the reflection of wave B over the lower symmetry surface) resulting in a strong distortion of the two waves (The indicated time advancement is computed from the shock impingement over the obstacle leading edge till the focusing).

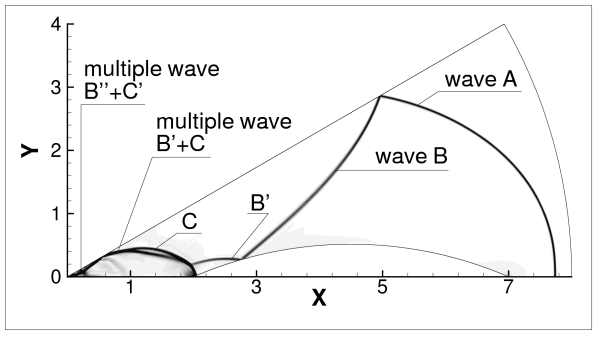

FIG. 25. Evolution of the reflections of waves B and C, which remain independent waves almost until the shock focusing ($N = 6$, $t/c = 0.21$, $r_{LE} = 7$, $\beta_P = 11$, $\frac{\tau}{\bar{\tau}} = 0.99$).

the distance between the leading edge and the upper reflecting surface depends also on the number of obstacles. However, a clear dependence of the reflection patterns on N was not observed.

6. *Total number of shock reflections*

Table VI reports the overall number of reflections affecting the shock before its focusing.

With the only exception of the 24-obstacle configuration, the number of total reflections before focusing increases with the number of obstacles. It is remarkable that the number of reflections appears to be almost independent on the initial pressure ratio β_P and on the obstacle thickness-to-chord ratio. For 24 obstacles at twice the reference distance, the number of reflections is lower than in the corresponding 16-obstacle cases. This is possibly due to the strong blockage effect which produces a nozzle-like flow in between each pair of obstacles. The supersonic flow in the divergent portion of the channel results in the onset of a new shock wave, here termed *nozzle shock*, as reported in figure 27. The new shock wave converges towards the focus and coalesces with the polygonal reshaped shock. After the coalescence, the shock undergoes a very limited number of reflections.

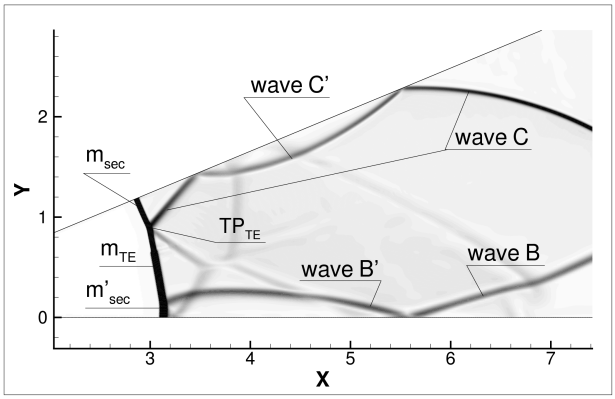

(a) $\frac{\tau}{\bar{\tau}} = 0.83$

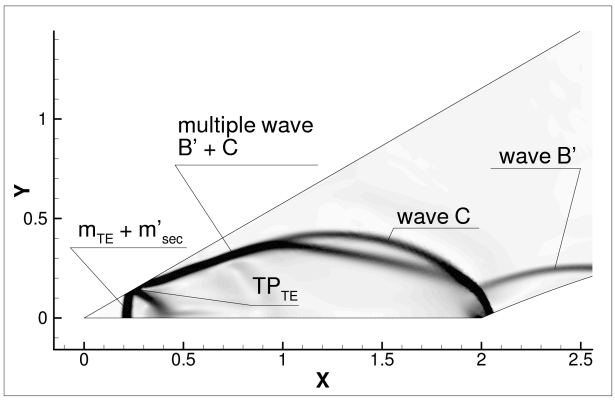

(b) $\frac{\tau}{\bar{\tau}} = 0.98$

FIG. 26. Reflection at the trailing edge approaching the symmetry line after the interaction with thick obstacles ($\beta_P = 11$): (a) reflected wave preceding the triple point ($N = 6$, $r_{LE} = 14$) and (b) vice-versa ($N = 8$, $r_{LE} = 14$).

TABLE V. Element which first reaches the symmetry surface: the reflected shock (RS) or the triple point (TP).

	r_{LE}	7			14			17.5		
β_P	N \ t/c	0.07	0.14	0.21	0.07	0.14	0.21	0.07	0.14	0.21
11	24			TP	TP	TP	RS			
	16	TP	TP	TP	TP	TP	RS	RS	RS	RS
	8	TP	TP	TP	TP	TP	RS	TP	RS	RS
	6	TP	TP	TP	TP	TP	RS	TP	TP	TP
16	24			TP	TP	TP	RS			
	16	TP	TP	TP	TP	TP	RS	RS	TP	RS
	8	TP	TP	TP	TP	TP	RS	TP	RS	TP
	6	TP	TP	TP	TP	TP	TP	TP	TP	RS
27	24			TP	TP	TP	RS			
	16	TP	TP	TP	TP	TP	RS	TP	RS	TP
	8	TP	TP	TP	TP	TP	RS	TP	RS	TP
	6	TP	TP	TP	TP	TP	TP	TP	TP	RS

TABLE VI. Global number of shock reflections (not including the focusing).

	r_{LE}	7			14			17.5		
β_P	N \ t/c	0.07	0.14	0.21	0.07	0.14	0.21	0.07	0.14	0.21
11	24			21	10	7	11			
	16	11	12	11	8	8	11	13	8	10
	8	7	7	6	7	7	8	8	8	8
	6	5	6	5	6	7	7	5	8	6
16	24			16	11	10	9			
	16	11	11	11	12	12	10	12	8	10
	8	5	6	5	7	7	7	9	7	7
	6	6	6	5	7	6	6	5	6	6
27	24			14	10	9	13			
	16	12	10	10	12	11	8	11	13	8
	8	5	6	5	7	7	7	7	7	6
	6	4	6	4	6	6	6	6	6	5

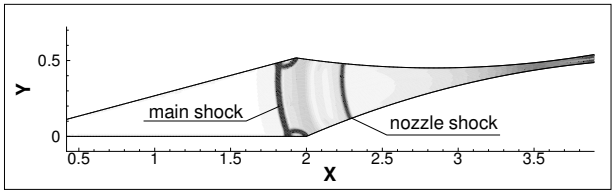

(a)

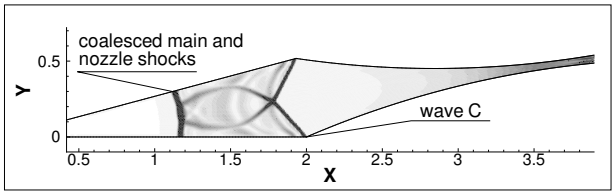

(b)

FIG. 27. Numerical Schlieren representing (a) the onset of a shock due to the nozzle effect behind the converging shock wave and (b) its coalescence with the converging shock reflections. The shock is depicted over a computational domain including two obstacles to highlight the nozzle effect ($\beta_P = 27$, $r_{LE} = 7$, $N = 24$, $t/c = 0.21$).

V. CONCLUSIONS

Numerical experiments were performed to assess the relevance of design parameters on the reshaping of cylindrical implosions converging in dilute air, with particular reference to the compression and temperature factors at the focus point.

The choice of considering aerodynamic obstacles as suggested in Ref. 13 allowed us to compute only the outer inviscid core and therefore results are independent from the considered length scale. Four parameters were studied: the initial compression factor, the number of obstacles, the leading-edge radial coordinate and the thickness-to-chord ratio of the profiles. Each of these factors was varied on three levels, generating a full factorial design. The correctness of the simulation results was assessed against the Guderley self similar solution

and experimental results from Ref. 13.

All the explored design parameters contribute to determine the final shock effectiveness and the reflection patterns. In particular, the incident shock Mach number was found to be very relevant to determine the effectiveness of the focusing process in terms of pressure and temperature factors, whereas at the same time it was shown to have a negligible influence in determining the reshaping pattern.

Considering first the energy focusing, an increase in the Mach number causes a more than proportional increase in the peak, in accordance with the ideal gas model. The configuration producing the highest temperature peak at the focus point consists of 16 obstacles with $\phi_c = 0.07$ and $r_{LE} = 14$, associated to a shock produced by an initial pressure ratio of 27. Indeed, the new configuration delivers an efficiency that is comparable to the one of the reference configurations, thus confirming the goodness of the obstacle arrangements proposed in Ref. 13.

Surprisingly, M_s turned out to be the less influential factor in the determination of reflection patterns occurring during the reshaping process, in terms of both number and type of reflections involved in the process. Diverse shock reflection configurations were highlighted, and locally compared, where possible, to the theoretical behavior of two-dimensional pseudo-steady ones. Shock reflection patterns were studied including the details of the leading edge reflections, the shock reshaping process, secondary reflections at the upper symmetry line and trailing edge reflections. Moreover, the total number of reflections up to the focus point and the trajectory of the triple point were reported.

REFERENCES

[1] R.W. Perry, A. Kantrowitz, *The production and stability of converging shock waves*, J. Appl. Phys. v. 22, pp. 878.886 (1951).

[2] B. P. Barber, S. J. Putterman, *Light scattering measurements of the repetitive supersonic implosion of a sonoluminescing bubble*, Phys. Rev. Lett., v. 69, pp. 38393842 (1992).

[3] J. D. Lindl, L. R. McCroy, E. M. Campbell, *Progress toward ignition and burn propagation in Inertial Confinement Fusion*, Phys. Today, pp. 32-40 (1992).

[4] K. Takayama, O. Onodera, Y. Hoshizawa, *Experiments on the stability of converging cylindrical shock waves*, Theor. Appl. Mech. v. 32, pp. 117127 (1984).

[5] S. H. R. Hosseini, K. Takayama, *Experimental study of the Richtmyer-Meshkov instability induced by cylindrical shock waves*, Phys. of Fluids v. 17 (2005).

[6] K. Takayama, H. Kleine, H. Grönig, *An experimental investigation of the stability of converging cylindrical shock waves in air*, Exp. in Fluids, v. 5, pp. 315-322 (1987).

[7] K. Fong, B. Ahlborn, *Stability of converging shock waves*, Phys. of Fluids v. 22, pp. 416-421 (1979).

[8] M. Kjellander, N. Tillmark, N. Apazidis, *Energy concentration by spherical converging shocks generated in a shock tube*, Phys. of Fluids v. 24 (2012).

[9] N. Apazidis, M. Kjellander, N. Tillmark, *High energy concentration by symmetric shock focusing*, Shock Waves v. 23, pp. 361-368 (2013).

[10] V. Eliasson, N. Apazidis, N. Tillmark, *Controlling the form of strong converging shocks by means of disturbances*, Shock Waves v. 17, pp. 29-42 (2007).

[11] V. Eliasson, *On focusing of shock waves*, Ph.D. dissertation, Department of Mechanics, KTH, Sweden (2007).

[12] H. Shi, K. Yamamura, *The interaction between shock waves and solid spheres arrays in a shock tube*, Acta Mech. Sinica v. 20-3, pp. 219-227 (2004).

[13] M. Kjellander, N. Tillmark, N. Apazidis, *Thermal radiation from a converging shock implosion*, Phys. of Fluids v. 22 (2010).

[14] Z. Zhai, T. Si, X. Luo, J. Yang, C. Liu, D. Tan, L. Zou, *Parametric study of cylindrical converging shock waves generated based on shock dynamics theory*, Phys. of Fluids v. 24 (2012).

[15] G. Ben-Dor, *Shock Wave Reflection Phenomena*, ed. Springer (1995).

[16] G. Guderley, *Starke kugelige zylindrische Verdichungsstöße in der Nähe des Kugelmittelpunktes bzw. der Zylinderachse*, Luftfahrtforschung v. 19, 302 (1942).

[17] F. Vignati, A. Guardone, *Multi-domain simulations of shock wave interaction with aerodynamic obstacles in cylindrical implosions*, J. Comp. and Appl. Math., v. 283, pp. 218227 (2015).

[18] H. Matsuo, *Converging shock waves generated by instantaneous energy release over cylindrical surfaces*, Phys. of Fluids v. 22, pp. 1618-1622 (1979).

[19] K. P. Stanyukovich, *Unsteady motion of Continuous Media*, Gostekhizdat, Moscow, pp. 804-878 (1955).

[20] J. H. Lee, B. H. K. Lee, *Cylindrical Imploding Shock Waves*, Phys. of Fluids v. 8, pp. 2148-2152 (1965).

[21] Z. Zhai, C. Liu, F. Qin, J. Yang, X. Luo, *Generation of cylindrical converging shock waves based on shock dynamics theory*, Phys. of Fluids v. 22, 041701 (2010).

[22] A. Guardone, D. De Santis, G. Geraci, M. Pasta, *On the relation between finite element and finite volume schemes for compressible flows with cylindrical and spherical symmetry*, J. Comp. Phys. v. 230 (3), pp. 680-694 (2011).

[23] D. Isola, A. Guardone, G. Quaranta, *Arbitrary Lagrangian Eulerian formulation for two-dimensional flows using dynamic meshes with edge-swapping*, J. Comp. Phys. v. 230, pp. 7706-7722 (2011).

[24] D. Isola, A. Guardone, G. Quaranta, *Finite-volume solution of two-dimensional compressible flows over dynamic adaptive grids*, J. Comp. Phys. v. 285, pp. 1-23 (2015).

[25] J. O. Langseth, R. J. LeVeque, *A wave propagation method for three-dimensional hyperbolic conservation laws*, J. Comp. Phys. v. 165, pp. 126-166 (2000).

[26] H. B. Callen, *Thermodynamics and an introduction to thermostatistics*, ed. John Wiley and sons, New York, (1985).

[27] M. Kjellander, N. Tillmark, N. Apazidis, *Shock dynamics of strong imploding cylindrical and spherical shock waves with real gas effects*, Phys. of Fluids v. 22, 116102 (2010)

[28] J. Tyl, E. Włodarczyk, *Analysis of imploding shock waves by the Chester-Chisnell-Witham method*, J. de Phys. Colloques, v. 45-C8, pp. 267-272 (1984).

[29] M. Van Dyke, A. J. Guttmann, *The converging shock wave from a spherical or cylindrical piston*, J. Fluid Mech. v. 120, pp. 451-462 (1982).

[30] H. Matsuo, *Cylindrically converging shock and detonation waves*, Phys. of Fluids v. 26, pp. 1755-1762 (1983).

[31] R. B. Payne, *A numerical method for a converging cylindrical shock*, J. Fluid Mech. v. 2-02, pp. 185-200 (1957).

[32] D. W. Schwendeman, G. B. Whitham, *On Converging Shock Waves*, Proc. Roy. Soc. A. v. 413, pp. 297-311 (1987).

[33] G. Ben-Dor, K. Takayama, *Application of steady shock polars to unsteady shock wave reflections*, AIAA J. v. 24, pp. 682-684 (1986).

[34] M. J. Lighthill, *The diffraction of blast I*, Proc. Roy. Soc. A. v. 198, pp. 454-470 (1948).

[35] P. Colella, L. F. Henderson, *The von Neumann paradox for the diffraction of weak shock waves*, J. Fluid Mech. v. 213, pp. 71-94 (1990).

[36] C. K. Law, I. I. Glass, *Diffraction of strong shock waves by a sharp compressive corner*, CASI Trans., v. 4, pp. 2-12 (1971).

[37] B. Schmidt, *Structure of Incipient Triple Point at the Transition from Regular Reflection to Mach Reflection*, in *Rarefied Gas Dynamics: Theoretical and Computational Techniques*, Progress in Astronautics and Aeronautics, v. 118, pp. 597-607 (1989).

[38] V. Eliasson, M. Kjellander, N. Apazidis, *Regular versus Mach reflection for converging polygonal shocks*, Shock Waves v. 17 (1-2), pp. 43-50 (2007).